

Detectability of dark matter density distribution via gravitational waves from binary black holes in the Galactic center

Zhijin Li^{1,4,5}, Xiao Guo^{1,*}, Zhoujian Cao^{1,3,†} and Yun-Long Zhang^{2,1‡}

¹*School of Fundamental Physics and Mathematical Sciences, Hangzhou Institute for Advanced Study, University of Chinese Academy of Sciences, Hangzhou 310024, China*

²*National Astronomical Observatories, Chinese Academy of Sciences, Beijing 100101, China*

³*Institute of Applied Mathematics, Academy of Mathematics and Systems Science, Chinese Academy of Sciences, Beijing 100190, China*

⁴*International Centre for Theoretical Physics Asia-Pacific (ICTP-AP), University of Chinese Academy of Sciences, Beijing 100049, China and*

⁵*CAS Key Laboratory of Theoretical Physics, Institute of Theoretical Physics, Chinese Academy of Sciences, Beijing 100190, China.*

The fundamental nature of dark matter (DM) remains unknown, with significant uncertainties in its density profile. DM environments surrounding massive binary black holes (BBHs) modify their orbital dynamics, thereby altering gravitational wave (GW) emissions. For BBH systems at the Galactic Center, dynamical friction induced by DM spikes could produce detectable deviations in GW spectra, potentially observable by future space-based detectors. To address the uncertainties in the Galactic Center's DM profile, we systematically examine two scenarios: the generalized Navarro-Frenk-White (gNFW) profile and its post-spike modification. We investigate the evolutionary effects of DM dynamical friction and accretion on the eccentricity and semi-latus rectum of secondary black holes (BHs) in elliptical orbits. By constructing orbital models with varying initial eccentricities across the mass-semi-latus rectum parameter space and utilizing 30 years of simulated pulsar timing array data from the Square Kilometer Array (SKA), we identify detectable parameter regimes of DM effects and employ these GW observational signatures to constrain different DM density profiles. Our analysis reveals that among gNFW profiles ($\gamma = 2, 1.5, 1, 0.5$), only $\gamma = 2$ produces significant detectable signatures. The formation of DM spikes further enhances these observable waveform deviations for all gNFW slopes.

CONTENTS

I. Introduction	2
II. Dark Matter Density Profile	3
A. Generalized NFW profile	3
B. Spike profile	4
III. Perturbed Kepler Orbits	5
A. Reaction of Gravitational Waves	7
B. Dynamical Friction and Accretion	8
C. Total Effect of Dark Matter	10
IV. Parameter Space Constraints	12
A. The SNR in PTA observations	13
B. Effects of gNFW profile	16
C. Effects of DM Spike Profile	17
V. Conclusions	19
Acknowledgments	21
A. Galactic Center Pulsar Timing Array (GC-PTA)	21
References	22

* guoxiao17@mailsucas.ac.cn

† zjcao@amt.ac.cn

‡ zhangyunlong@nao.ac.cn

I. INTRODUCTION

A wealth of observational evidence provides robust support for the existence of dark matter (DM) [1–3]. Nevertheless, its fundamental nature remains one of the most pressing and profound mysteries in modern physics, while its density profile continues to be a subject of intense scientific interest. Through the cosmological N -body numerical simulations, Navarro, Frenk and White (NFW) obtained a universal density profile for DM halos, called NFW profile [4, 5]. The NFW profile exhibits a density scaling of $\rho(r) \sim r^{-1}$ at small scales, while subsequent studies suggested a steeper slope of $\rho(r) \sim r^{-1.5}$ [6, 7], leading to cuspy distributions in the central regions. However, there is no conclusive evidence for such steep inner density slopes, the simulations for the NFW profile and the Einasto profile do not match well on small scales [8]. Instead, observations favor the existence of a “core” where the DM distribution becomes relatively flat, the so-called core-cusp problem [9–11].

It has been demonstrated that if a supermassive black hole (SMBH) (with mass regime 10^6 – $10^9 M_\odot$) is embedded in a DM halo [12], its adiabatic compression of the surrounding DM inevitably produces a high-density, concentrated spike [12]. The resulting density profile follows $\rho(r) \sim r^{-\gamma_{\text{sp}}}$, with a significantly steeper slope in the range $2.25 \leq \gamma_{\text{sp}} \leq 2.5$. Besides, the dynamical processes such as major merger events of seed host galaxies and gravitational scattering by stars may lead to the destruction or reduction of DM spikes [13–15]. The Galactic Center (GC), our closest galactic nucleus, hosts a SMBH (Sgr A*) [16–19]. This unique astrophysical laboratory provides unprecedented opportunities to study DM properties/distributions and test general relativity. The DM distribution in the inner Galactic region remains poorly understood due to the lack of direct observational data and the limited resolution of numerical simulations (below ~ 1 kpc). Recent studies suggest that Sgr A* has not experienced major mergers in the past 10 Gyr [20, 21], making the existence of a DM spike around Sgr A* uncertain. Although the Milky Way’s (MW) DM distribution has been investigated through rotation curve analyses [22–25], constraining its inner profile (within \sim kpc scales) remains challenging [26]. The distribution of DM in the inner Galactic region remains an open question, as the environment near the central BH is highly complex and may involve interactions with baryonic matter. Additionally, the nature of DM itself introduces significant uncertainties in its density profile.

On the other hand, the intermediate-mass black holes (IMBHs) may exist around Sgr A* within certain parameter ranges [19, 27–33]. Such an IMBH would form a binary black hole (BBH) system with Sgr A*, with orbital periods ranging from months to years. The resulting gravitational wave (GW) emission falls within the nHz– μ Hz frequency range, detectable by pulsar timing arrays (PTAs) [34–43]. The GW signals from this system may exhibit detectable differences due to DM environmental effects compared to DM-free scenarios, potentially serving as a probe for mapping the DM distribution in the GC. Since 2015, LIGO’s GW detections have inaugurated the era of GW astronomy [44–47]. Recent observations by the NANOGrav [48, 49], Parkes PTA [50], Chinese PTA [51], and European PTA [52] collaborations have reported evidence (2–4 σ confidence level) for a stochastic gravitational wave background (SGWB) in the nanohertz frequency range. These findings present both new opportunities and challenges [53] for investigating DM distribution in the GC region. The future Square Kilometer Array (SKA) is projected to detect new stable millisecond pulsars (MSPs) and form a high-sensitivity PTA [54, 55], designated as the SKA-PTA. In the near future, GW observations could potentially reveal the DM distribution in the GC.

The presence of DM subjects compact objects moving through it to dynamical friction [56, 57]. Eda et al. [58, 59] pioneered the investigation of how dynamical friction from DM mini-spikes affects intermediate-mass-ratio inspirals (IMRIs) - GW sources potentially detectable by LISA in the future. Macedo et al. [60] examined a compact object traversing a DM region, where the quasi-adiabatic inspiral is primarily dominated by dynamical friction and accretion rather than GW radiation. An IMRI system consisting of an intermediate-mass black hole (IMBH) and a smaller BH, when accounting for GW radiation, dynamical friction, and accretion within the minispikes, can influence the GW phase and inspiral period [61]. The dynamical friction from a DM minispikes within an IMRI system will increase the eccentricity of the elliptical orbit [62]. A halo feedback mechanism is proposed in which a secondary object loses energy while moving through a DM spike, depositing this energy into the surrounding DM. This process reduces the DM density, consequently weakening the dynamical friction effect [63].

The presence of a DM minispikes in an IMRI system introduces additional orbital precession, leading to a detectable phase shift in the GW waveform [64]. Taking into account the velocity distribution of DM particles relative to the small BH, the dynamical friction induced by the DM spike would circularize the elliptical orbit [65]. In extreme-mass-ratio inspirals (EMRIs), dynamical friction can significantly alter gravitational waveforms in the frequency domain [66, 67], while a DM halo may reduce precession rates or even reverse their direction [68]. Reference [69] investigated the influence of DM distributions under relativistic conditions on BBH systems, [70, 71] examined the effects of baryonic matter accretion disks, [72] analyzed the case of slowly rotating Kerr BHs, while [73] studied the impact of DM spikes surrounding SMBHs on inspiral dynamics.

In this paper, we investigate the dynamical evolution of secondary BHs orbiting within the DM halo surrounding the SMBH at the GC. Their orbital dynamics are influenced by both dynamical friction and DM accretion effects. Focusing on the GC’s DM density profile, we address current uncertainties in its inner slope and the potential existence of a DM

spike by comparing two scenarios: (1) a generalized NFW profile without spike ($\gamma = 0.5-2.0$), and (2) a spike-modified profile accounting for DM enhancement. We systematically analyze how these DM distributions affect the orbital evolution (eccentricity and semi-latus rectum) and corresponding GW signatures. By exploring the parameter space of secondary BH masses and orbital parameters, we quantify DM-induced deviations in GW waveforms compared to DM-free scenarios. These findings could enable measurement of the DM density slope, providing constraints on DM models and insights into the nature of DM.

The paper is organized as follows. In Section II, we introduce the generalized NFW profile for the MW's DM distribution and subsequently derive its spike-like modification resulting from adiabatic compression within the gravitational influence radius of the SMBH. In Section III, we examine two distinct dynamical effects: DM accretion by secondary BHs and the resulting orbital element evolution induced by DM dynamical friction. In Section IV, we explore the observable parameter space where DM effects on secondary BHs become significant and evaluate the prospects for detecting these effects in future GW observations. Finally, we draw conclusions and discussion in Section V.

II. DARK MATTER DENSITY PROFILE

In this section, we investigate the SMBH at the center of the MW galaxy, which is enveloped by a DM halo. Since the internal DM distribution remains uncertain, particularly regarding the presence or absence of a spike, we consider two distinct DM density profiles: a gNFW profile without a spike and a spike-modified profile.

A. Generalized NFW profile

The DM halo density profiles are often approximated by the NFW profile [5]

$$\rho_{\text{NFW}}(r) = \frac{\rho_0}{(r/r_s)(1+r/r_s)^2}, \quad (1)$$

where r_s represents the typical scale radius, ρ_0 denotes the typical scale density. One has to determine the parameters r_s and ρ_0 that enter in the tentative DM distributions $\rho(r)$. Various methodologies exist for determining the distribution of DM within galaxies. One such approach involves extracting DM parameters from numerical simulations of galactic halos. Alternatively, the DM profile can be derived by imposing specific constraints on the galactic structure. In this study, we employ the latter method, ensuring that our model aligns with empirical data and theoretical expectations. The distance from the Sun to the center of the MW galaxy is about 8 kpc (kiloparsecs) [74, 75], and the DM density near the Sun is [26, 76, 77]

$$\rho(r_\odot) = \rho_\odot = 0.4 \text{ GeV/cm}^3 \approx 0.0106 M_\odot/\text{kpc}^3. \quad (2)$$

The total mass of DM within the MW, including that contained within the virial radius r_{200} is [77, 78]

$$M_{DM}^{200} \approx 1.0 \times 10^{12} M_\odot. \quad (3)$$

For the MW, virial radius r_{200} is approximately 200 to 300 kpc. Therefore, we can consider M_{DM}^{200} as the total DM mass contained within a large sphere of radius 200 kpc, centered around the center of the Galaxy. We take the DM density around the Sun and the DM contained within the virial radius of the MW (approximately 200 kpc) with a mass of $10^{12} M_\odot$ as constraints. In order to consider various models of DM distribution, we generalize the DM distribution to the gNFW (generalized NFW) profile [79]

$$\rho_{\text{gNFW}}(r) = \frac{\rho_0}{(r/r_s)^\gamma(1+r/r_s)^{3-\gamma}}. \quad (4)$$

Using the constraints provided by Eqs. (2) and (3), we obtain the following two equations

$$\rho_{\text{gNFW}}(r_\odot) = 0.0106 M_\odot/\text{kpc}^3, \quad (5)$$

and

$$\int_{r_{\text{ISCO}}}^{200\text{kpc}} \rho_{\text{gNFW}}(r) dr = 1.0 \times 10^{12} M_\odot. \quad (6)$$

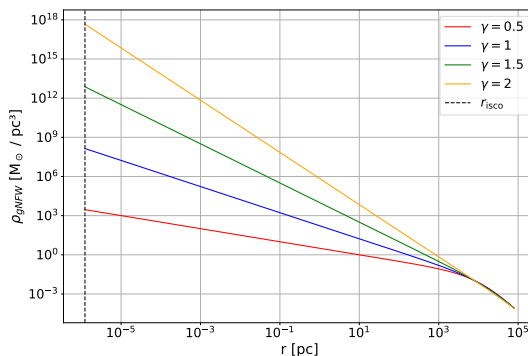


FIG. 1: The DM density profiles for the gNFW halo in Eq. (4) are illustrated in the figure. The possible gNFW profile of DM in our MW is represented by a solid red line for $\gamma = 0.5$, a blue line for $\gamma = 1$, a yellow line for $\gamma = 1.5$, and a yellow line for $\gamma = 2$. At the center of the MW, there exists a SMBH with a mass of $4.26 \times 10^6 M_\odot$. As one approaches the GC, the DM distribution becomes increasingly dense for different indices. However, within the innermost stable circular orbit, the DM distribution is assumed to be zero.

Here, r_{ISCO} represents the innermost stable circular orbit (ISCO) of the central SMBH, given by $r_{\text{ISCO}} = 3R_s = \frac{6Gm_1}{c^2}$, where $m_1 = 4.26 \times 10^6 M_\odot$ is the mass of Sgr A* [17, 18, 75, 80, 81]. In this context, for the gNFW profile, we adopt a range for γ such that $0.5 \leq \gamma \leq 2$. The DM density inside r_{ISCO} is assumed to be zero. Using Eqs. (5) and (6), we solve for the indices $\gamma = 0.5, 1, 1.5, 2$ and compute the corresponding values of r_s and ρ_0 , as shown in Table I. Following this, we use the data from the Table I to plot the gNFW density profiles for various slopes, which are displayed in Fig. 1.

γ	0.5	1	1.5	2
r_s (pc)	12754.12	19191.47	36818.52	181453.85
ρ_0 (M_\odot/pc^3)	0.0283	0.00887	0.00144	0.0000215

TABLE I: Values of the parameters r_s and ρ_0 of the gNFW profile in Eq. (4) for different power-law indices γ , obtained by solving Eqs. (5) and (6).

B. Spike profile

Gondolo and Silk [12] pointed out that the adiabatic growth of the SMBH at the center of the DM halo will significantly increase the DM density within its gravitational influence radius $r_{\text{sp}} \sim 0.2r_h$ [82]. Here, r_h is the radius of gravitational influence of the SMBH, defined by the equation $4\pi \int_0^{r_h} \rho(r) r^2 dr = 2m_1$, where m_1 is mass of Srg A*. In this study, we assume that the DM distribution at the outer region of the SMBH in the MW is described by the gNFW profile, whereas within the gravitational influence radius r_{sp} it follows a spike distribution

$$\rho_{\text{spike}}(r) = \rho_{\text{sp}} \left(1 - \frac{4R_s}{r}\right)^3 \left(\frac{r_{\text{sp}}}{r}\right)^{\gamma_{\text{sp}}}. \quad (7)$$

Here, ρ_{sp} denotes a density at a reference radius r_{sp} , $R_s = 2Gm_1/c^2$ is the Schwarzschild radius of the SMBH with mass m_1 and

$$\gamma_{\text{sp}} = (9 - 2\gamma)/(4 - \gamma). \quad (8)$$

To sum up, the final density profile of a halo is composed of three layers

$$\rho(r) = \begin{cases} 0, & r \leq r_{\text{ISCO}}, \\ \rho_{\text{sp}} \left(1 - \frac{4R_s}{r}\right)^3 \left(\frac{r_{\text{sp}}}{r}\right)^{\gamma_{\text{sp}}}, & r_{\text{ISCO}} < r \leq r_{\text{sp}}, \\ \rho_{\text{gNFW}}(r), & r_{\text{sp}} < r. \end{cases} \quad (9)$$

γ	0.5	1	1.5	2
γ_{sp}	16/7	7/3	2.4	2.5
r_{sp} (pc)	27.309	12.664	3.289	0.192
ρ_{sp} (M_{\odot}/pc^3)	6.216	13.425	1.705×10^3	1.929×10^7

TABLE II: In the gNFW profile in Eq. (4) with $\gamma = \{0.5, 1, 1.5, 2\}$, the adiabatic growth of the central BH leads to the formation of a DM spike in Eq. (7). The corresponding values of $\gamma_{\text{sp}} = \{16/7, 7/3, 2.4, 2.5\}$, r_{sp} , and ρ_{sp} after the formation of the DM spike are recorded in the table.

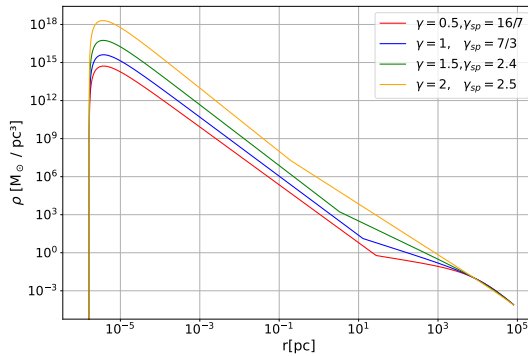


FIG. 2: In the gNFW profile in Eq. (4), the power-law indices $\gamma = \{0.5, 1, 1.5, 2\}$ correspond to the formation of spike power-law indices $\gamma_{\text{sp}} = \{16/7, 7/3, 2.4, 2.5\}$ in Eq. (9). The relevant parameters are listed in Table II.

Next, we need to determine the two parameters of the DM spike distribution, r_{sp} and ρ_{sp} . By ensuring that the DM densities of inner spike profile and the outer gNFW profile are equal at $r = r_{\text{sp}}$, we can use this matching condition to derive $\rho_{\text{sp}} = \rho_{\text{gNFW}}(r_{\text{sp}})/(1 - 4R_s/r_{\text{sp}})^{-3}$. Here we assume that the distribution of DM around the BH initially follows a gNFW profile. The adiabatic growth of the BH produces a dense spike in the inner region of the minihalo within a radius of r_{sp} . The gravitational influence radius can be denoted as $4\pi \int_0^{r_h} \rho_{\text{gNFW}}(r) r^2 dr = 2m_1$ [82]. Taking into account the influence radius of gravity and the constraints imposed by the matching condition at r_{sp} , we obtain the following system of equations

$$\rho_{\text{sp}} = \frac{\rho_{\text{gNFW}}(r_{\text{sp}})}{(1 - 4R_s/r_{\text{sp}})^3}, \quad (10)$$

and

$$4\pi \int_0^{r_h} \rho_{\text{gNFW}}(r) r^2 dr = 2m_1. \quad (11)$$

For $\gamma = 0.5, 1, 1.5, 2$ in Eq. (4), we list the relevant calculation results in Table II.

In Fig. 2, we observe the formation of spike distributions under different initial power-law indices γ . Specifically, when the initial distribution follows an NFW profile in Eq. (1) with $\gamma = 1$, the resulting spike exhibits a power-law index of $\gamma_{\text{sp}} = 7/3$. For the initial power-law index in the range $1 \leq \gamma \leq 2$, the corresponding spike indices fall within $2.25 \leq \gamma_{\text{sp}} \leq 2.5$. Comparing with the gNFW profiles in Figure 1, we note that in the absence of a spike, the DM density profiles near the GC exhibit significant discrepancies for different power-law indices. However, after the formation of a spike, the slope and density variations become more pronounced for distributions with smaller initial γ values. Furthermore, the differences in DM density near the GC among spikes with different power-law indices are considerably smaller compared to the case without a spike.

III. PERTURBED KEPLER ORBITS

In this section, we present the method of osculating orbits. The BBH system is composed of a primary mass, denoted as m_1 , and a secondary mass, m_2 , both idealized as Schwarzschild BHs for simplicity, as illustrated in Fig. 3.

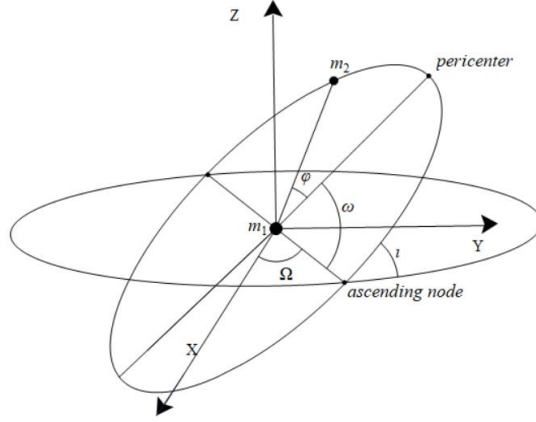


FIG. 3: The schematic diagram of orbital motion viewed in the fundamental reference frame.

Within this framework, we consider a scenario where a smaller BH undergoes Keplerian motion around the SMBH located at the center of the MW. The Keplerian orbit is described by the following equation

$$r = \frac{p}{1 + e \cos(\varphi)}, \quad (12)$$

where r is the radial distance, p is the semi-latus rectum, e is the orbital eccentricity, and φ is the true anomaly. The radial and angular velocities of a Keplerian orbit are given by

$$\dot{r} = \sqrt{\frac{Gm}{p}} e \sin(\varphi), \quad (13)$$

$$\dot{\varphi} = \sqrt{\frac{Gm}{p^3}} [1 + e \cos(\varphi)]^2, \quad (14)$$

where $m := m_1 + m_2$ is the total mass of the system.

While exact analytical solutions do not exist for the three-body or many-body problems, in certain cases where the gravitational influence of additional bodies is sufficiently weak, the system can be treated as a perturbed two-body problem. The relative acceleration of two bodies in a Keplerian orbit is given by [83]

$$\mathbf{a} = -\frac{Gm}{r^2} \mathbf{n} + \mathbf{f}, \quad (15)$$

where $\mathbf{r} := \mathbf{r}_1 - \mathbf{r}_2$ is the relative position vector, $\mathbf{n} := \mathbf{r}/r$ is the unit radial vector, and \mathbf{f} represents the perturbing force per unit mass. The perturbing force can be expressed as

$$\mathbf{f} = \mathcal{R} \mathbf{n} + \mathcal{S} \mathbf{k} + \mathcal{W} \mathbf{e}_z, \quad (16)$$

where \mathbf{k} is the unit vector orthogonal to \mathbf{n} , and \mathbf{e}_z is the normal vector to the orbital plane.

The equations governing the osculating orbital elements are given by

$$\frac{dp}{dt} = 2\sqrt{\frac{p^3}{Gm}} \frac{1}{1 + e \cos \varphi} \mathcal{S}, \quad (17)$$

$$\frac{de}{dt} = \sqrt{\frac{p}{Gm}} \left[\sin \varphi \mathcal{R} + \frac{2 \cos \varphi + e(1 + \cos^2 \varphi)}{1 + e \cos \varphi} \mathcal{S} \right], \quad (18)$$

$$\begin{aligned} \frac{d\varphi}{dt} &= \sqrt{\frac{Gm}{p^3}} (1 + e \cos \varphi)^2 \\ &+ \frac{1}{e} \sqrt{\frac{p}{Gm}} \left[\cos \varphi \mathcal{R} - \frac{2 + e \cos \varphi}{1 + e \cos \varphi} \sin \varphi \mathcal{S} \right]. \end{aligned} \quad (19)$$

Here, we assume that the orbital elements ω and ι are both zero. When the perturbative force is very small, such that the changes in the orbital elements are minimal, it is convenient to use φ as the independent variable instead of t . Under this approximation, the non-Keplerian terms on the right-hand side of the equations can be neglected, allowing for a good approximation of the orbital dynamics. By combining Eqs. (17), Eq. (18) and Eq. (19), and expanding to the first-order term in $p^2/(Gm)$, we obtain

$$\frac{dp}{d\varphi} = 2 \frac{p^3}{Gm} \frac{1}{(1 + e \cos \varphi)^3} \mathcal{S}, \quad (20)$$

$$\frac{de}{d\varphi} = \frac{p^2}{Gm} \left[\frac{\sin \varphi}{(1 + e \cos \varphi)^2} \mathcal{R} + \frac{2 \cos \varphi + e(1 + \cos^2 \varphi)}{(1 + e \cos \varphi)^3} \mathcal{S} \right], \quad (21)$$

$$\frac{dt}{d\varphi} = \sqrt{\frac{p^3}{Gm}} \frac{1}{(1 + e \cos \varphi)^2} \left\{ 1 - \frac{1}{e} \frac{p^2}{Gm} \times \left[\frac{\cos \varphi}{(1 + e \cos \varphi)^2} \mathcal{R} - \frac{(2 + e \cos \varphi) \sin \varphi}{(1 + e \cos \varphi)^3} \mathcal{S} \right] \right\}. \quad (22)$$

For Eq. (22), since $p^2/(Gm) \ll 1$, the contribution of the second term can be neglected, yielding

$$\frac{dt}{d\varphi} = \sqrt{\frac{p^3}{Gm}} \frac{1}{(1 + e \cos \varphi)^2}. \quad (23)$$

The perturbing force per unit mass \mathbf{f} , induces both oscillations and secular changes in the orbital elements. To quantify the cumulative drift associated with these secular effects, we average over a complete orbital period. The orbital average of $\langle \dot{a} \rangle$ is defined as

$$\left\langle \frac{da}{dt} \right\rangle = \frac{1}{T} \int_0^P \frac{da}{dt} dt = \frac{1}{T} \int_0^{2\pi} \frac{da}{d\varphi} d\varphi, \quad (24)$$

where T denotes the orbital period.

A. Reaction of Gravitational Waves

GWs carry away the orbital energy of binary systems, acting as a reaction force that diminishes the orbital eccentricity and drives the orbits closer together. This reaction can be treated as a perturbative force, and its effect on the acceleration of the system is given by [83]

$$\mathbf{a}_{\text{GW}} = \frac{8}{5} \frac{G^2 m \mu}{c^5 r^3} \left[\left(3v^2 + \frac{17}{3} \frac{Gm}{r} \right) \dot{r} \mathbf{n} - \left(v^2 + 3 \frac{Gm}{r} \right) \mathbf{v} \right], \quad (25)$$

where $\mu = m_1 m_2 / (m_1 + m_2)$ is the reduced mass.

At the lowest order in a post-Newtonian expansion and using the quadrupole formula, the standard results yield the expressions for the secular changes in the semi-latus rectum and eccentricity e due to GW emission [83, 84]

$$\left\langle \frac{dp}{dt} \right\rangle_{\text{GW}} = -\frac{8}{5} \eta \frac{(Gm)^3}{c^5 p^3} (1 - e^2)^{3/2} (8 + 7e^2), \quad (26)$$

$$\left\langle \frac{de}{dt} \right\rangle_{\text{GW}} = -\frac{8}{5} \eta \frac{(Gm)^3}{c^5 p^4} (1 - e^2)^{3/2} \left(\frac{304}{24} e + \frac{121}{24} e^3 \right), \quad (27)$$

where $\eta = m_1 m_2 / (m_1 + m_2)^2$ is the symmetric mass ratio, and the subscript ‘‘GW’’ indicates that these effects arise from the reaction of GWs. From Eqs. (26) and (27), it is evident that GW emission leads to a gradual reduction in both the semi-latus rectum and the eccentricity of the binary system.

B. Dynamical Friction and Accretion

Chandrasekhar [56] proposed that an object moving through an infinite, homogeneous medium experiences a drag force due to gravitational interactions, acting in the direction opposite to its velocity. This effect, known as dynamical friction, depends on the velocity of the moving object, as well as the density and sound speed of the surrounding medium [57, 85]. The SMBH at the center of the MW is surrounded by a DM halo. In this scenario, we consider a small BH orbiting the SMBH while moving through the DM medium. As a result, the small BH will experience dynamical friction. Without loss of generality, we focus on the supersonic regime, where the dynamical friction force can be expressed as

$$\mathbf{f}_{\text{DF}} = -\frac{4\pi G^2 m_2^2 \rho_{\text{DM}} I_v}{v^3} \mathbf{v}, \quad (28)$$

where \mathbf{v} is the velocity of the small BH, which can be decomposed into $\mathbf{v} = \dot{r}\mathbf{n} + r\dot{\varphi}\mathbf{k}$. Here, I_v is the Coulomb logarithm $I_v = \left\{3, 10, \log \sqrt{\frac{m_1}{m_2}}\right\}$ [59, 62, 63], which depends on the velocity v and the sound speed of the DM halo. In this work, we adopt $I_v = \log\left(\sqrt{\frac{m_1}{m_2}}\right)$.

Eq. (28) can be rewritten as

$$\mathbf{f}_{\text{DF}} = -\frac{4\pi G^2 m_2^2 \rho_{\text{DM}} I_v}{v^3} (\dot{r}\mathbf{n} + r\dot{\varphi}\mathbf{k}). \quad (29)$$

Substituting the above equation into Eqs. (20), (21), and combining with Eq. (24), we obtain the following equations:

$$\begin{aligned} \left\langle \frac{dp}{dt} \right\rangle_{\text{DF}} &= -\frac{1}{T} \int_0^{2\pi} 2 \frac{p^3}{Gm} \frac{1}{(1+e\cos\varphi)^3} \\ &\quad \times \left(\frac{4\pi G^2 m_2 \rho_{\text{DM}} I_v}{v^3} r\dot{\varphi} \right) d\varphi \\ &= -\int_0^{2\pi} \frac{4G^{1/2} m_2 \rho_{\text{DM}} I_v p^{5/2}}{(1-e^2)^{-3/2} m^{3/2}} f(\varphi) d\varphi, \end{aligned} \quad (30)$$

where $f(\varphi) = \frac{1}{(1+e\cos\varphi)^2 (e^2+2e\cos\varphi+1)^{3/2}}$,

$$\begin{aligned} \left\langle \frac{de}{dt} \right\rangle_{\text{DF}} &= -\frac{1}{T} \int_0^{2\pi} \frac{p^2}{Gm} \times \\ &\quad \left[\frac{2\cos\varphi + e(1+\cos^2\varphi)}{(1+e\cos\varphi)^3} \left(\frac{4\pi G^2 m_2 \rho_{\text{DM}} I_v}{v^3} r\dot{\varphi} \right) \right. \\ &\quad \left. + \frac{\sin\varphi}{(1+e\cos\varphi)^2} \left(\frac{4\pi G^2 m_2 \rho_{\text{DM}} I_v}{v^3} \dot{r} \right) \right] d\varphi \\ &= -\int_0^{2\pi} \frac{4p^{3/2} G^{1/2} m_2 \rho_{\text{DM}} I_v}{(1-e^2)^{-3/2} m^{3/2}} g(\varphi) d\varphi, \end{aligned} \quad (31)$$

where $g(\varphi) = \frac{e+\cos\varphi}{(1+e\cos\varphi)^2 (e^2+2e\cos\varphi+1)^{3/2}}$.

We now turn to the discussion of accretion. As the small BH moves through the DM environment, it will accrete DM. In our analysis, we assume that the mass of the small BH does not exceed 1% of the mass of central SMBH. This allows us to neglect the disruption of the DM distribution caused by the accretion of the small BH. In this study, we assume that the radius of the small BH exceeds the mean free path of DM particles. Furthermore, we focus exclusively on non-annihilating DM particles, neglecting all interactions other than gravitational effects. Under these conditions, the accretion process of the small BH is described by Bondi-Hoyle accretion. Consequently, the mass flux at the event horizon of the small BH is given by [60, 86]

$$\dot{m}_2 = 4\pi G^2 \lambda \frac{m_1^2 \rho_{\text{DM}}}{(v^2 + c_s^2)^{3/2}}, \quad (32)$$

where λ is a dimensionless parameter of order unity, dependent on the properties of the DM medium, and c_s denotes the sound speed of the DM medium. For simplicity, we assume $v \gg c_s$ and adopt $\lambda = 1$ throughout this work.

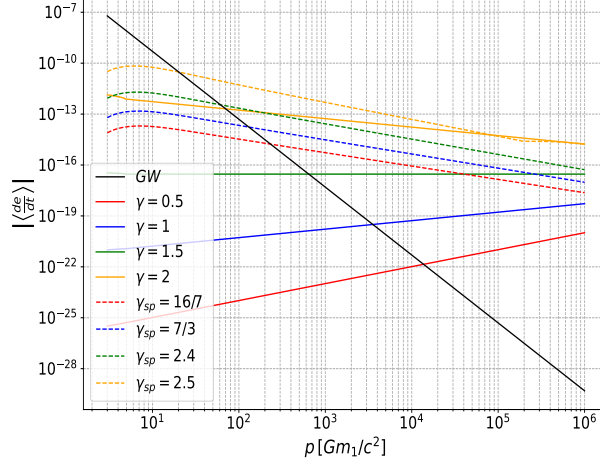


FIG. 4: The variation of $|\langle \frac{de}{dt} \rangle|$ with respect to the initial semi-latus rectum $p = p_0$ is analyzed, where we assume $e = 0.6$ and $m_2 = 1000 M_\odot$. The solid black line represents the eccentricity change due to GWs, with $|\langle \frac{de}{dt} \rangle_{\text{GW}}|$ in Eq. (27). The solid line corresponds to the rate of eccentricity change $|\langle \frac{de}{dt} \rangle_{\text{AC}}|$ in Eq. (36) for the gNFW profile in Eq. (4), and the dashed line represents the case for a DM spike in Eq. (7).

Due to the accretion of DM, the equation of motion can be written as

$$m_2 \dot{\mathbf{v}} + \dot{m}_2 \mathbf{v} = -\frac{Gm_1 m_2}{r^3} \mathbf{r}, \quad (33)$$

where the force arising from the accretion term $\dot{m}_2 \mathbf{v}$ is given by

$$\mathbf{f}_{\text{AC}} = -\frac{4\pi G^2 m_2^2 \rho_{\text{DM}} \lambda}{v^3} \mathbf{v}. \quad (34)$$

Substituting the above expressions into Eqs. (20), (21), and combining with Eq. (24), we obtain the following equations

$$\begin{aligned} \left\langle \frac{dp}{dt} \right\rangle_{\text{AC}} &= -\frac{1}{T} \int_0^{2\pi} 2\sqrt{\frac{p^3}{Gm}} \frac{1}{1+e\cos\varphi} \\ &\quad \times \left(\frac{4\pi G^2 m_2 \rho_{\text{DM}} \lambda}{v^3} r \dot{\varphi} \right) d\varphi \\ &= -\int_0^{2\pi} \frac{4G^{1/2} m_2 \rho_{\text{DM}} \lambda p^{5/2}}{(1-e^2)^{-3/2} m^{3/2}} f(\varphi) d\varphi, \end{aligned} \quad (35)$$

where $f(\varphi) = \frac{1}{(1+e\cos\varphi)^2 (e^2+2e\cos\varphi+1)^{3/2}}$,

$$\begin{aligned} \left\langle \frac{de}{dt} \right\rangle_{\text{AC}} &= -\frac{1}{T} \int_0^{2\pi} \frac{p^2}{Gm} \times \\ &\quad \left[\frac{\sin\varphi}{(1+e\cos\varphi)^2} \left(\frac{4\pi G^2 m_2 \rho_{\text{DM}} \lambda}{v^3} \dot{r} \right) + \right. \\ &\quad \left. \frac{2\cos\varphi + e(1+\cos^2\varphi)}{(1+e\cos\varphi)^3} \left(\frac{4\pi G^2 m_2 \rho_{\text{DM}} \lambda}{v^3} r \dot{\varphi} \right) \right] d\varphi \\ &= -\int_0^{2\pi} \frac{4p^{3/2} G^{1/2} m_2 \rho_{\text{DM}} \lambda}{(1-e^2)^{-3/2} m^{3/2}} g(\varphi) d\varphi, \end{aligned} \quad (36)$$

where $g(\varphi) = \frac{e+\cos\varphi}{(1+e\cos\varphi)^2 (e^2+2e\cos\varphi+1)^{3/2}}$.

From Eqs. (26) and (27), we see that gravitational radiation decreases both the eccentricity e and the orbital semi-latus rectum p . For dynamical friction and accretion, as shown in Eqs. (28) and (34), they share the same functional form. Through Eqs. (30) and (35), we observe that they reduce the semi-latus rectum p and accelerate the merger. However, for the eccentricity evolution, since it involves the term $g(\varphi) = \frac{e + \cos \varphi}{(1 + e \cos \varphi)^2 (e^2 + 2e \cos \varphi + 1)^{3/2}}$, the numerator in the integral can become negative, potentially leading to an increase in eccentricity. Given that the forces generated by dynamical friction and accretion have identical structures, we focus exclusively on studying the effect of accretion on eccentricity.

As illustrated in Fig. 4, we investigate the rate of eccentricity change $\langle \frac{de}{dt} \rangle$, for an initial eccentricity $e_0 = 0.6$, using the initial semi-latus rectum p_0 as the independent variable to examine how $\langle \frac{de}{dt} \rangle$ varies with p_0 . We compare $|\langle \frac{de}{dt} \rangle_{\text{GW}}|$ and $|\langle \frac{de}{dt} \rangle_{\text{AC}}|$, where the absolute values are taken because $\langle \frac{de}{dt} \rangle_{\text{GW}}$ is negative. Our findings reveal that at larger BBH separations, the rate of eccentricity change is primarily dominated by accretion, with the effect becoming more pronounced as the DM density increases. For gNFW DM distributions in Eq. (4), significant differences arise depending on the power-law index. For $\gamma = 2$, the accretion begins to dominate over GW radiation at $p_0 \approx 100 Gm_1/c^2$. For $\gamma = 0.5$, accretion reaches a magnitude comparable to GW radiation at $p_0 \approx 10000 Gm_1/c^2$. When DM forms a spike, its effect becomes significant around $p_0 \approx 100 Gm_1/c^2$.

C. Total Effect of Dark Matter

In this subsection, we comprehensively consider the effects of dynamical friction, accretion, and GW radiation reaction as perturbations on the eccentricity and semi-latus rectum of the small BH. Here, we neglect the influence of the DM gravitational potential, and the force per unit mass acting on the small BH is given by

$$\bar{\mathbf{a}}_{\text{tot}} = \mathbf{a}_{\text{DF}} + \mathbf{a}_{\text{AC}} + \mathbf{a}_{\text{GW}}. \quad (37)$$

Since the three forces mentioned above are treated as perturbations, we still approximate the motion of the secondary object as following an elliptical orbit. The rate of change of φ with respect to time is given by

$$\frac{d\varphi}{dt} = \sqrt{\frac{Gm}{p^3}} (1 + e \cos \varphi)^2. \quad (38)$$

The general expressions for the semi-latus rectum p and eccentricity e are as follows

$$\left\langle \frac{dp}{dt} \right\rangle_{\text{tot}} = \left\langle \frac{dp}{dt} \right\rangle_{\text{DF}} + \left\langle \frac{dp}{dt} \right\rangle_{\text{AC}} + \left\langle \frac{dp}{dt} \right\rangle_{\text{GW}}, \quad (39)$$

$$\left\langle \frac{de}{dt} \right\rangle_{\text{tot}} = \left\langle \frac{de}{dt} \right\rangle_{\text{DF}} + \left\langle \frac{de}{dt} \right\rangle_{\text{AC}} + \left\langle \frac{de}{dt} \right\rangle_{\text{GW}}. \quad (40)$$

Taking into account the combined effects of dynamical friction, accretion, and GW radiation, we have plotted the changes in eccentricity e and semi-latus rectum p of a small BH under the generalized gNFW model. As shown in Fig. 5, the red, blue, green, and yellow curves represent the temporal evolution of the semi-latus rectum p and eccentricity e under different DM density profiles characterized by $\gamma \in \{0.5, 1, 1.5, 2\}$, considering only the pure gNFW profile without accounting for potential DM spike formation near the BHs.

The orbital evolution for systems with initial semi-latus rectum $p_0 = 1000 Gm_1/c^2$ ($\sim 0.2\text{mpc}$) exhibits characteristic behavior, where in the absence of DM (black curves), the orbital decay proceeds exclusively through GW emission. When DM is included, the orbital decay rate increases significantly for steeper density profiles ($\gamma \geq 1.5$), with a clear separation visible between the $\gamma = 2$ and $\gamma = 1.5$ cases throughout their evolution. For shallower profiles ($\gamma \leq 1$), the effects become progressively weaker: while the $\gamma = 1$ case shows marginally detectable deviations upon close inspection, the $\gamma = 0.5$ profile remains practically indistinguishable from the DM free scenario.

The eccentricity evolution shown in the lower panel of Fig. 5 demonstrates a similar dependence on the γ parameter. The steep $\gamma = 2$ profile produces significant eccentricity enhancement, while $\gamma = 1.5$ shows a modest but discernible increase. Profiles with $\gamma \leq 1$ demonstrate no measurable eccentricity modification compared to the vacuum case. These results collectively indicate that dynamical friction effects scale monotonically with the central density slope, where only sufficiently steep gNFW profiles ($\gamma \geq 1.5$) generate observable perturbations to both the orbital decay

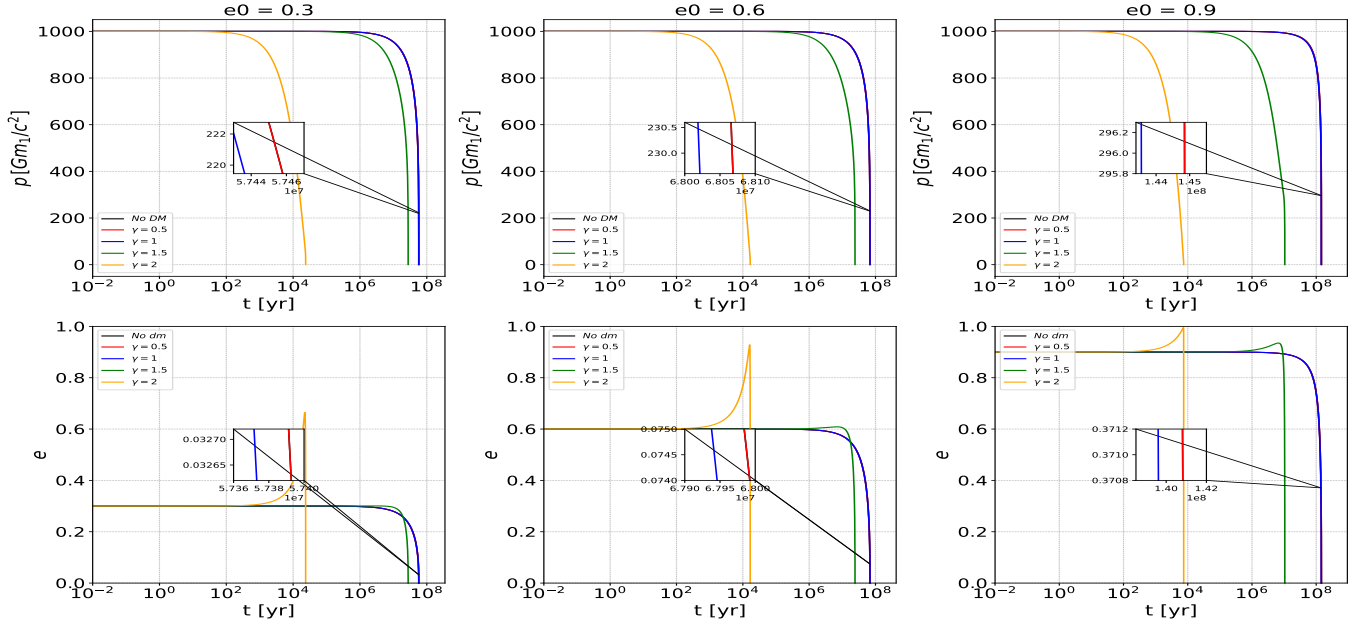


FIG. 5: This figure presents the temporal evolution of eccentricity and semi-latus rectum p for BBH systems embedded in a gNFW profile of DM distribution in Eq. (4) with slope $\gamma = \{0.5, 1, 1.5, 2\}$. The initial eccentricities e_0 are $\{0.3, 0.6, 0.9\}$ for each case. The top row shows the evolution of the semi-latus rectum p with time, while the bottom row displays the corresponding eccentricity evolution. In all panels, the black curves represent the reference case without DM. For the plots of semi-latus rectum p (top row), the horizontal axis shows time in years (yr), and the vertical axis is normalized in units of Gm_1/c^2 . The initial semi-latus rectum is set to $p_0 = 1000 Gm_1/c^2$, where $m_1 = 4.26 \times 10^6 M_\odot$ is the primary BH mass and the secondary has a mass of $m_0 = 1000 M_\odot$.

rate and eccentricity evolution, while shallower profiles ($\gamma \leq 1$) remain observationally degenerate with the pure GW emission scenario at current detection thresholds.

For an initial semi-latus rectum of $p_0 = 5000 Gm_1/c^2$ (~ 1 mpc), Fig. 6 reveals several key features of the orbital evolution. The top panels demonstrate that the orbital decay rates for $\gamma = 1$ and $\gamma = 0.5$ become distinguishable, while the $\gamma = 0.5$ case initially appears degenerate with the dark-matter-free scenario. However, detailed inspection of magnified regions confirms their subtle but measurable separation. Notably, this wider binary separation ($p_0 = 5000 Gm_1/c^2$) provides better discrimination between different DM profile slopes γ compared to the $1000 Gm_1/c^2$ case. The eccentricity evolution exhibits more pronounced DM effects at larger orbital scales. Compared to the case of $p_0 = 1000 Gm_1/c^2$, the $\gamma = 2$ density profile produces significantly stronger eccentricity enhancement, while $\gamma = 1.5$ shows substantial increase and $\gamma = 1$ displays modest but detectable growth. This systematic dependence on both γ and initial orbital separation suggests that wider binaries are more sensitive probes of the DM density profile's inner slope.

As evident from Fig. 5, the yellow and blue curves exhibit close proximity during their initial descent, while their separation becomes increasingly pronounced with higher initial eccentricity. In Fig. 6, we also observe that the blue and red curves remain close to each other at small eccentricities, but gradually diverge as the initial eccentricity increases. For the initial semi-latus rectum $p_0 = 1000 Gm_1/c^2$, we observe that the merger times for $\gamma = 2$ and $\gamma = 1.5$ decrease with increasing initial eccentricity, while the blue curve in the figure shows an increase in merger time. When the initial semi-latus rectum is $p_0 = 5000 Gm_1/c^2$, the figure reveals that the merger times for $\gamma = 2$, $\gamma = 1.5$, and $\gamma = 1$ all decrease with growing initial eccentricity, whereas for $\gamma = 0.5$ the merger time increases.

Our results indicate a significant modification of the standard gNFW DM profile near the GC SMBH. Through adiabatic compression, the profile transforms into a steeper spike configuration with enhanced density distribution. The original gNFW power-law indices $\gamma \in \{0.5, 1, 1.5, 2\}$ evolve into corresponding spike indices $\gamma_{\text{sp}} \in \{16/7, 7/3, 2.4, 2.5\}$. Fig. 7 shows the orbital evolution of a secondary BH with an initial semi-latus rectum p of $p_0 = 1000 Gm_1/c^2$. Compared to the case without a DM spike (Fig. 5), we observe that the formation of a DM spike significantly enhances both dynamical friction and accretion effects. In the absence of a spike, the profiles with $\gamma = 1$ and 0.5 are nearly identical to the no-dark-matter case. When a DM spike forms, steeper profiles with higher γ_{sp} values exhibit more pronounced environmental effects, showing faster orbital semi-latus rectum decay in denser DM environments and more significant eccentricity enhancement compared to the no-spike case, where both effects intensify with increasing

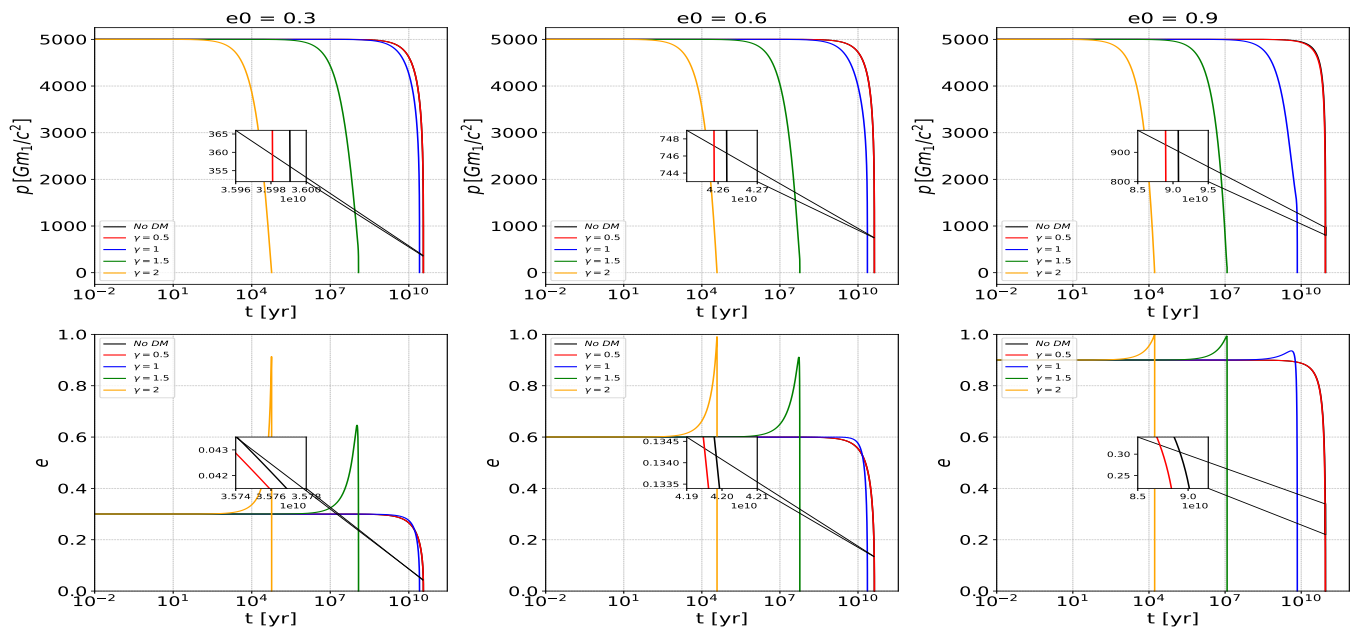


FIG. 6: Orbital evolution for a binary system with a secondary BH mass of $10^3 M_\odot$ and initial semi-latus rectum $p_0 = 5000 Gm_1/c^2$. The top row shows the temporal evolution of the semi-latus rectum p for three different initial eccentricities: $e_0 \in \{0.3, 0.6, 0.9\}$. The bottom row displays the corresponding eccentricity evolution for the same set of initial conditions, illustrating how both orbital parameters evolve differently depending on the initial eccentricity configuration.

γ_{sp} .

For an initial semi-latus rectum of $p_0 = 1000 Gm_1/c^2$, we observe that different initial eccentricities $e_0 = \{0.3, 0.6, 0.9\}$ have negligible impact on the total merger duration across various power-law profiles. The eccentricity evolution shows distinct patterns: when $e_0 = 0.3$, $\gamma_{\text{sp}} = \{16/7, 7/3, 2.4, 2.5\}$ produces $\Delta e \sim \{0.1, 0.2, 0.3, 0.4\}$; for $e_0 = 0.6$, the maximum $\Delta e \sim \{0.1, 0.2, 0.25, 0.3\}$; while $e_0 = 0.9$ yields only $\Delta e \sim 0.1$. This clearly demonstrates that systems with lower initial eccentricities undergo more substantial relative changes in eccentricity during their evolution, with the effect diminishing as the initial eccentricity increases.

For systems with initial semi-latus rectum $p_0 = 5000 Gm_1/c^2$, comparison of Figs. 7 and 8 shows that while increasing the initial p by a factor of 5 results in a 10^3 longer merger timescale without DM, the presence of a DM spike reduces this increase to just 1 order of magnitude, demonstrating the significant acceleration of BBH coalescence through DM dynamical friction and accretion. The environmental effects dominate over GW emission at larger separations, primarily driving eccentricity enhancement, with $\gamma_{\text{sp}} = \{16/7, 7/3, 2.4, 2.5\}$ producing eccentricity differences $\Delta e \sim \{0.3, 0.4, 0.5, 0.6\}$ for $e_0 = 0.3$, while systems with $e_0 = 0.9$ all exhibit eccentricity growth to nearly 1 followed by rapid decay to 0.

Throughout the evolution, the DM spike formation leads to clearly distinguishable BBH dynamics for different γ_{sp} values (see Figs. 7–8). For gNFW profiles without spike formation around the SMBH, distinguishing DM distributions with $\gamma < 1$ would require larger initial p_0 parameters.

IV. PARAMETER SPACE CONSTRAINTS

Our previous investigation comprehensively analyzed the full temporal evolution of both the semi-latus rectum p and eccentricity e in BBH systems, though the required observational timescale for such processes exceeds practical feasibility. This section instead examines the behavior of a secondary BH moving along an elliptical orbit within a DM environment, focusing on whether orbit modifications caused by DM dynamical friction and accretion over a 30-year timescale could be detectable through GW observations, while simultaneously providing constraints on the DM power-law distribution.

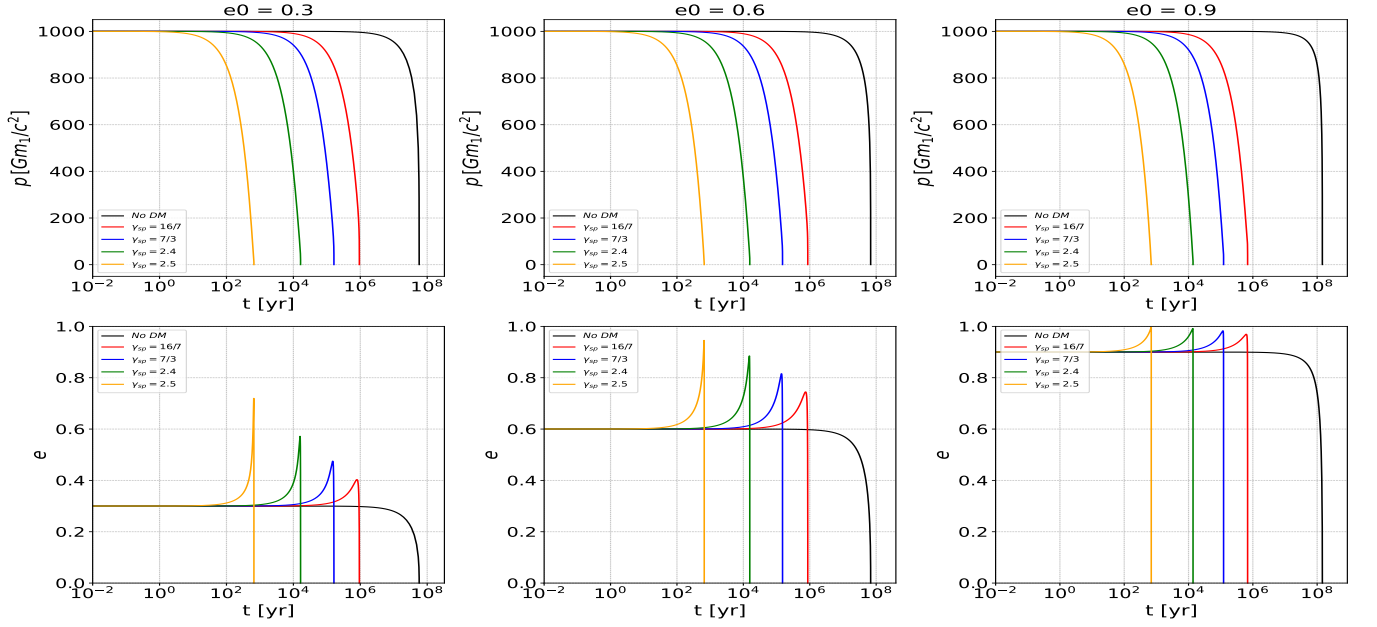


FIG. 7: Orbital evolution of a secondary BH in a DM spike environment with the profile in Eq. (7). The DM density profile is modeled as a spike-modified gNFW profile in Eq. (9), formed through adiabatic compression by the central SMBH. **Top row:** Temporal evolution of the semi-latus rectum p (in units of Gm_1/c^2) with time in years (yr). **Bottom row:** Corresponding eccentricity evolution. Initial conditions are fixed at $p_0 = 1000 Gm_1/c^2$ with increasing initial eccentricities (left to right: $e_0 = 0.3, 0.6, 0.9$).

A. The SNR in PTA observations

The waveform of GWs is produced from the inspiral of a binary system. If such a BBH system exists at the GC with orbital periods ranging from months to years, the resulting GWs would have frequencies from μHz to nHz , potentially detectable by PTAs. The plus and cross modes are given by [87, 88]

$$\begin{aligned}
 h_+ = & -\frac{2G^2 m \mu}{c^4 p R} (1 + \cos^2 \iota) \left\{ \left[\cos(2\phi + 2\omega) \right. \right. \\
 & + \frac{5e}{4} \cos(\phi + 2\omega) + \frac{e}{4} \cos(3\phi + 2\omega) - \frac{e^2}{2} \cos 2\omega \\
 & \left. \left. + \frac{e}{2} \sin^2 \iota (\cos \phi + e) \right] \right\}, \tag{41}
 \end{aligned}$$

$$\begin{aligned}
 h_\times = & -\frac{4G^2 m \mu}{c^4 p R} \cos \iota \left[\sin(2\phi + 2\omega) + \frac{5e}{4} \sin(\phi + 2\omega) \right. \\
 & \left. + \frac{e}{4} \sin(3\phi + 2\omega) + \frac{e^2}{2} \sin 2\omega \right], \tag{42}
 \end{aligned}$$

where m is the total mass of the system and μ denotes the reduced mass. The parameter R represents the distance from the BBH's center of mass to the observer; in our analysis, this corresponds to the separation between the MW's GC and the solar system. The angle between the binary's orbital angular momentum axis and the detector's line of sight is denoted by ι , while ω describes the azimuthal component of the inclination angle. For simplicity, we adopt $\iota = 0$ and $\omega = 0$ throughout this work.

Fig. 9 shows the GW waveform of a binary BH system. The primary BH is the supermassive BH at the center of the MW, and the secondary BH has a mass of $1000M_\odot$, with an initial eccentricity of $e_0 = 0.6$ and semi-latus rectum of $p_0 = 1000 Gm_1/c^2$. The black solid line represents the case without DM, the red solid line corresponds to a gNFW profile with $\gamma = 2$, and the blue line shows the DM spike distribution with $\gamma_{\text{sp}} = 2.5$. The top panel displays the GW over 30 years, while the bottom panel zooms in on years 25 to 26.

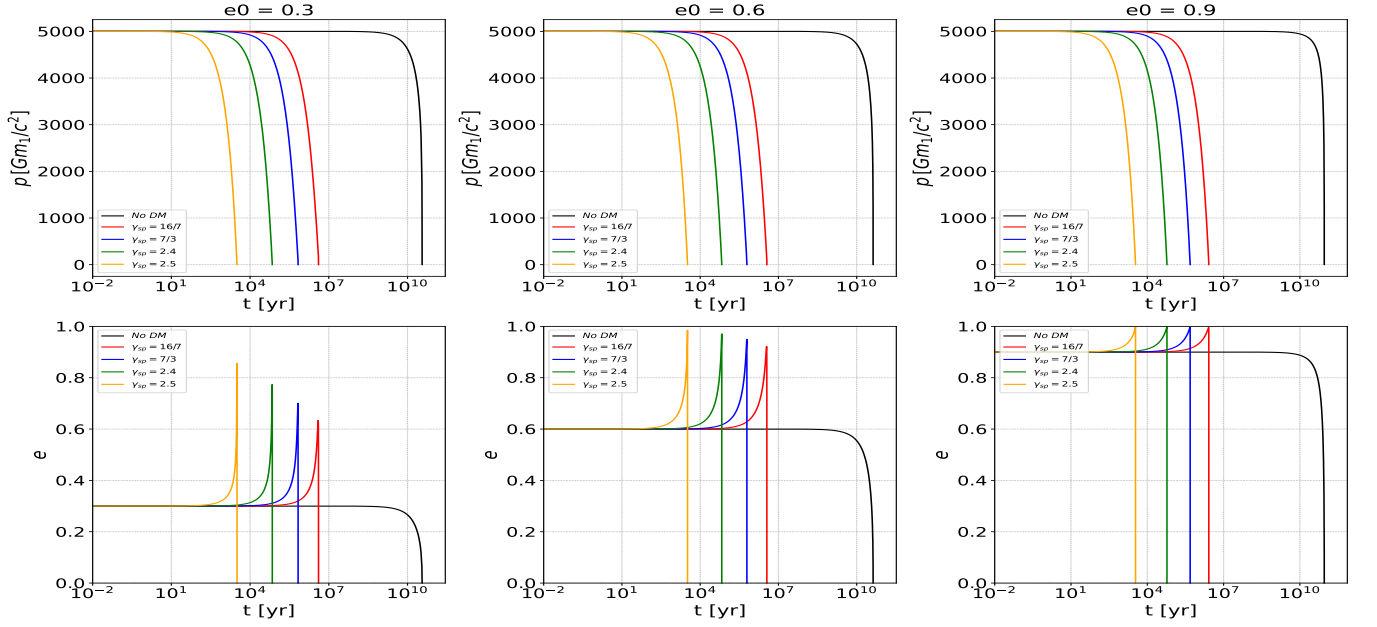


FIG. 8: Orbital evolution of a secondary BH in a DM spike environment with the profile in Eq. (7). Initial conditions are fixed at $p_0 = 5000 Gm_1/c^2$ with increasing initial eccentricities (from left to right: $e_0 = 0.3, 0.6, 0.9$).

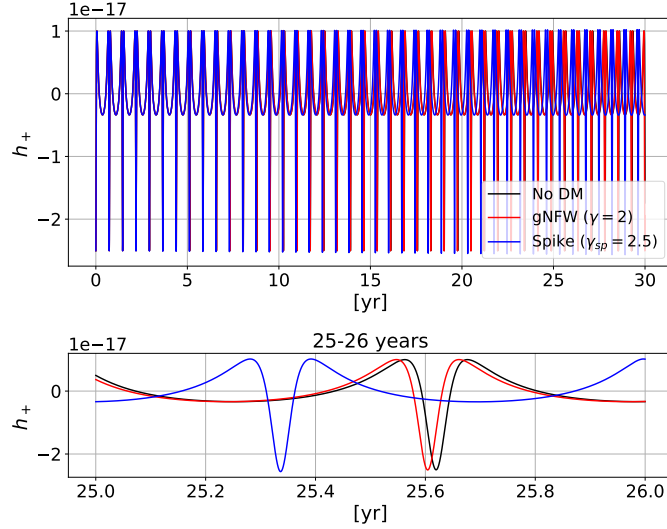


FIG. 9: GW strain h_+ comparison for different DM profiles in Eq. (4) and Eq. (7). The black line is GW waveform without the influence of DM. The red (blue) line represents GW waveform under influence of DM with gNFW (spike) density profile. Top: Full evolution over 30 years. Bottom: Zoomed view of years 25-26.

In the frequency domain, the GW waveform is given by

$$\tilde{h}_{+, \times}(f) = \int_{-\infty}^{\infty} h_{+, \times}(t) e^{2\pi i f t} dt. \quad (43)$$

Given two signals $h_1(t)$ and $h_2(t)$, we can define the inner product $(h_1|h_2)$ as

$$(h_1|h_2) \equiv 4\text{Re} \int_{f_{\min}}^{f_{\max}} \frac{\tilde{h}_1(f)\tilde{h}_2^*(f)}{S_n(f)} df. \quad (44)$$

where Re denotes the real part, $f_{\min} = 1/T_{\text{obs}}$, and $f_{\max} = 1/\Delta t$. The GW frequency range that can be probed by a

PTA is limited by the cadence (Δt) and the total observation period (T_{obs}), i.e., $1/T_{\text{obs}} \lesssim f \lesssim 1/\Delta t$. Current PTAs normally set a cadence of $\Delta t \sim 1 - 2$ weeks and have been running for a total observation period of $T_{\text{obs}} \sim 30$ years.

We define the effective signal-to-noise ratio (SNR) ϱ [89] by

$$\varrho^2 = (h|h) = 4 \int_{f_{\min}}^{f_{\max}} df \frac{|\tilde{h}_+(f)|^2 + |\tilde{h}_\times(f)|^2}{S_n(f)}. \quad (45)$$

For a PTA with N_p (≥ 3) MSPs, two different data processing approaches exist for SNR estimation, namely the matched filtering method and the cross-correlation method. In this work, we adopt the matched filtering approach, which yields the following SNR expression [90]

$$\varrho^2 = \sum_{i=1}^{N_p} 4\chi_i^2 \int_{f_{\min}}^{f_{\max}} df \frac{|\tilde{h}_+(f)|^2 + |\tilde{h}_\times(f)|^2}{S_{n,i}(f)}. \quad (46)$$

For convenience, the total SNR used for theoretical analysis may be approximated as

$$\varrho^2 \simeq 4N_p\chi^2 \int_{f_{\min}}^{f_{\max}} df \frac{|\tilde{h}_+(f)|^2 + |\tilde{h}_\times(f)|^2}{S_n(f)}. \quad (47)$$

By assuming that all MSPs contribute to the SNR equally [91], here, χ represents the geometric factor, which equals 0.365 under the far-field approximation [90].

We consider the noise affecting PTA detection of individual sources to be primarily composed of two components: the shot noise and the confusion with the gravitational wave background (GWB) [92–94]. For this analysis, we neglect the intrinsic red noises of pulsars [95, 96]. The power spectral density (PSD) of the GWB strain originating from shot noise is typically characterized as [97]

$$S_{n,s}(f) = 8\pi^2\sigma^2 f^2 \Delta t, \quad (48)$$

where σ is the root mean square (RMS) of pulsar timing residuals noise, Δt is the mean cadence of the PTA observations and we set $N_p = 1000$, $\sigma = 100$ ns, $\Delta t = 0.02$ yr, $T = 30$ yr for SKA-PTA. The strain of GWB due to GW radiation from numerous distant MBBHs can be described as [94]

$$h_b = \mathcal{A} \frac{(f/1\text{yr}^{-1})^{-2/3}}{[1 + (f_{\text{bend}}/f)^{\kappa_{\text{gw}}\gamma_{\text{gw}}}]^{1/(2\gamma_{\text{gw}})}}. \quad (49)$$

We adopt $\log \mathcal{A} \sim -15.70$, $f_{\text{bend}} = 2.45 \times 10^{-10}$ Hz, $\kappa_{\text{gw}} = 3.74$, $\gamma_{\text{gw}} = 0.19$ which are the median values for the GWB predictions in [90, 94]. The total noise for individual PTA sources is then

$$S_n(f) = S_{n,s} + \frac{h_b^2}{f}, \quad (50)$$

or in the strain form as

$$h_n(f) = \sqrt{fS_{n,s} + h_b^2}. \quad (51)$$

In our the SNR calculations, we treat the GWB as a noise component.

The two waveforms are indistinguishable if the condition [98]

$$(\delta h|\delta h) = (h_1 - h_2|h_1 - h_2) < 1. \quad (52)$$

In practical observations, when $h_1 \approx h_2$, the aforementioned formula can be simplified. Conventionally, researchers compute a quantity called the ‘‘Fitting Factor’’ (FF) [99, 100], defined as

$$\text{FF} = \frac{(h_1|h_2)}{\sqrt{(h_1|h_1)(h_2|h_2)}}, \quad (53)$$

and compare it with a threshold FF defined as and compare it with a threshold FF defined as

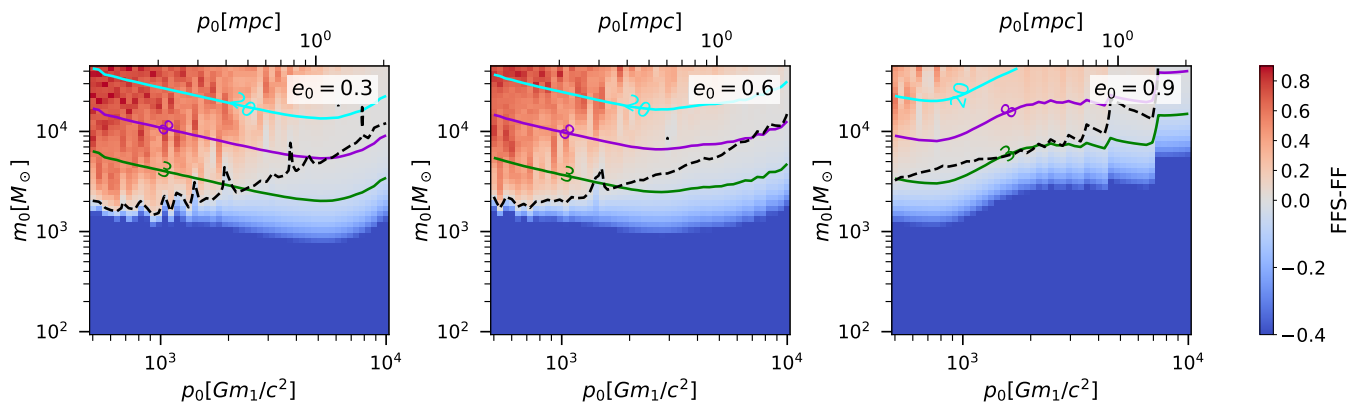


FIG. 10: The secondary BHs orbiting the SMBH at the GC, where the DM distribution follows a gNFW profile in Eq. (4) with $\gamma = 2$, emit GWs potentially detectable by SKA-PTA. The analysis shows the parameter space with the horizontal axis representing the semi-latus rectum p_0 , in units of $R_1 = Gm_1/c^2$ ranging from $500R_1$ to $1000R_1$ (approximately 0.1mpc to 2mpc), and the vertical axis shows the secondary BH mass m_0 in solar mass units, spanning from $100M_\odot$ to $42600M_\odot$. The top axis is the semi-latus rectum p_0 labeled in mpc. Black dashed contours indicate the $\text{FFS}-\text{FF} = 0$ isoline. The SNR contours are displayed as green curves for $\text{SNR} = 3$, purple for $\text{SNR} = 8$, and cyan for $\text{SNR} = 15$. The three panels present results for different initial orbital eccentricities with $e_0 = 0.3$ at left, $e_0 = 0.6$ at center, and $e_0 = 0.9$ at right. The color gradient represents $\text{FFS}-\text{FF}$ values, where red regions indicate $\text{FFS}-\text{FF} > 0$, blue regions show $\text{FFS}-\text{FF} < 0$, and silver-white areas correspond to $\text{FFS}-\text{FF} \approx 0$.

$$\text{FFS} = 1 - \frac{1}{(h_1|h_1) + (h_2|h_2)}. \quad (54)$$

The quantity FFS is intrinsically connected to the SNR, defined as $\text{SNR} = \sqrt{(h|h)}$. When $h_1 \simeq h_2$, this relationship simplifies to $\text{FFS} \simeq 1 - 1/(2\text{SNR}^2)$. Under this approximation, the criterion in Eq. (52) reduces to $\text{FF}-\text{FFS} > 0$, which serves as the condition for waveform indistinguishability.

In BBH systems, the presence of DM significantly alters the dynamics. While pure GW radiation reaction dominates the smaller BH's motion in DM-free environments, additional effects - particularly dynamical friction and accretion - must be considered when DM is present.

The distinguishability of gravitational waveforms depends critically on the $\text{FF}-\text{FFS}$ value:

- When $\text{FFS}-\text{FF} < 0$, the GW waveforms with and without DM influence become indistinguishable.
- When $\text{FFS}-\text{FF} > 0$, the GW waveforms can be clearly distinguished.

B. Effects of gNFW profile

Our analysis focuses on DM's impact on the inspiral phase of the smaller BH within binary systems. Using PTA detection ranges [101], we explore the SNR distribution across the parameter space of mass and semi-latus rectum p , identifying regions where DM most significantly affects the $\text{FFS}-\text{FF}$ relationship. We investigate GWs from BBH using SKA-PTA observations with a total duration of 30 years. Assuming a gNFW profile in Eq. (4) around the SMBH at the GC without considering spike formation, we search within the PTA sensitivity range to identify the parameter space where the effects of dynamical friction and accretion from DM are most significant while remaining detectable through GW observations.

Fig. 10 displays our analysis results for the $\gamma = 2$ scenario, illustrating the $\text{FFS}-\text{FF}$ values via a color gradient as functions of the semi-latus rectum p_0 (on the horizontal axis) and the secondary BH mass m_0 (on the vertical axis). The fitting factor FF serves as a quantitative measure of waveform similarity between systems with and without DM effects, where higher FF values indicate greater similarity and consequently weaker DM influence. The threshold $\text{FFS}-\text{FF}$ determines the critical boundary for observable waveform differences, with red regions where $\text{FFS}-\text{FF} > 0$ representing detectable differences whose magnitude correlates with color intensity, blue regions where $\text{FFS}-\text{FF} < 0$ corresponding to negligible differences, and silvery-white areas near zero indicating borderline cases requiring extended observation

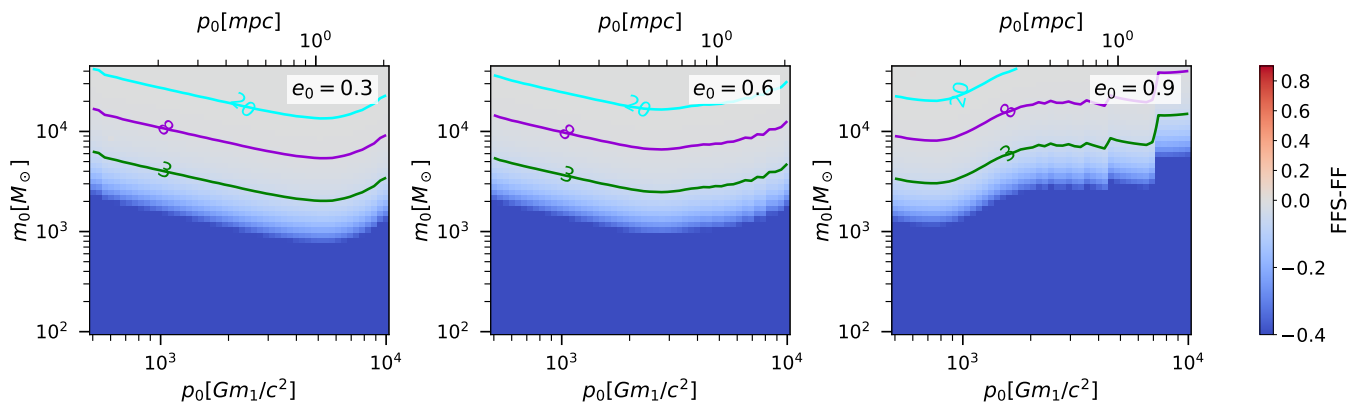


FIG. 11: The detection analysis for the DM density profile with $\gamma = 1.5$ indicates that across all cases of initial orbital eccentricities from $e_0 = 0.3$ to 0.9 , the parameter space exhibits predominantly silvery-white distribution characteristics. The labels are the same as described in Fig. 10. This observation suggests marginal detectability of waveform differences during the 30-year observation period. The figure shows $\text{FFS-FF} \lesssim 0$ throughout, with no $\text{FFS-FF} = 0$ contour line present.

periods. The black dashed contour marks the $\text{FFS-FF} = 0$ level while green, purple and cyan contours denote SNR of 3, 8 and 20 respectively. The three panels systematically present results for initial orbital eccentricities of 0.3 in the left panel, 0.6 in the central panel, and 0.9 in the right panel.

For Fig. 10 with initial eccentricity $e_0 = 0.3$, scattered black dots appear above the $\text{SNR}=8$ contour, corresponding to FFS-FF values approaching zero with minor fluctuations and measurement uncertainties. For the cases with eccentricities $e_0 = 0.3$ and 0.6 , the waveforms show significant differences when the semi-latus rectum $p_0 \lesssim 0.5$ mpc and mass $m_0 \gtrsim 2000 M_\odot$. To detect such cases requires $m_0 \gtrsim 4000 M_\odot$ for $\text{SNR} > 3$, while precise observation of this event demands $\text{SNR} > 8$, which in turn requires $m_0 \gtrsim 8000 M_\odot$. Although SKA-PTA is more sensitive to slightly larger semi-latus rectum values, this region appears silver-white with FFS-FF approaching zero, making it unsuitable as our detection zone. The most eccentric case with $e_0 = 0.9$ demonstrates detectable differences only for masses surpassing $10^4 M_\odot$, exhibiting both diminished spatial extent and intensity of red regions along with an upward shift of the zero contour that reduces the detectable parameter space.

The analysis reveals non-monotonic color variations with noticeable fluctuations within red regions, accompanied by corresponding undulations in the zero contour. Measurement precision improves with higher SNR, and the combination of parameter space above both the zero contour and the $\text{SNR}=8$ threshold provides optimal detection conditions. Based on comprehensive examination of these results, we conclude that selecting regions with SNR exceeding 8 yields the most reliable waveform difference detection.

For the DM distribution with $\gamma = 1.5$ shown in Fig. 11, we observe significant differences compared to the $\gamma = 2$ case. Notably, during SKA-PTA's 30-year observation window, the entire parameter space of semi-latus rectum $p_0 \in [500 Gm_1/c^2, 10^4 Gm_1/c^2]$ and compact object masses $m_0 \gtrsim 1000 M_\odot$ appears silvery-white. When plotting the $\text{FFS-FF}=0$ contour line, it does not appear in the figure because $\text{FFS-FF} \lesssim 0$ throughout the silvery-white region, indicating no detectable waveform differences across the entire parameter space for $\gamma = 1.5$.

If we could establish a GC-PTA consisting of 10 MSPs within our galaxy, it would enable exploration of a larger parameter space and increase the FFS threshold to reveal more subtle waveform differences. The detection results using GC-PTA are presented in the Appendix A. As shown in the gNFW profile with $\gamma = 2$ in Fig. 16 in the Appendix A, using GC-PTA detection, a mass close to $100 M_\odot$ can be detected at a semi-latus rectum around 0.2 mpc with an eccentricity of 0.3, while a mass of approximately $200 M_\odot$ can be detected at an eccentricity of 0.6. For an eccentricity of 0.9, a mass of $5000 M_\odot$ can be detected. GC-PTA significantly expands the detectable parameter space. For the distribution with $\gamma = 1.5$, we cannot detect the waveform differences even when using GC-PTA, so we do not present it in the Appendix A.

C. Effects of DM Spike Profile

This study investigates DM spike structures in Fig. 2 formed through adiabatic compression around the MW's central BH, a process that significantly enhances the DM density distribution. For spikes $\gamma_{\text{sp}} = 2.5$ generated from gNFW profiles with $\gamma = 2$, Fig. 12 shows that compared to the no-spike scenario, the red region expands and darkens,

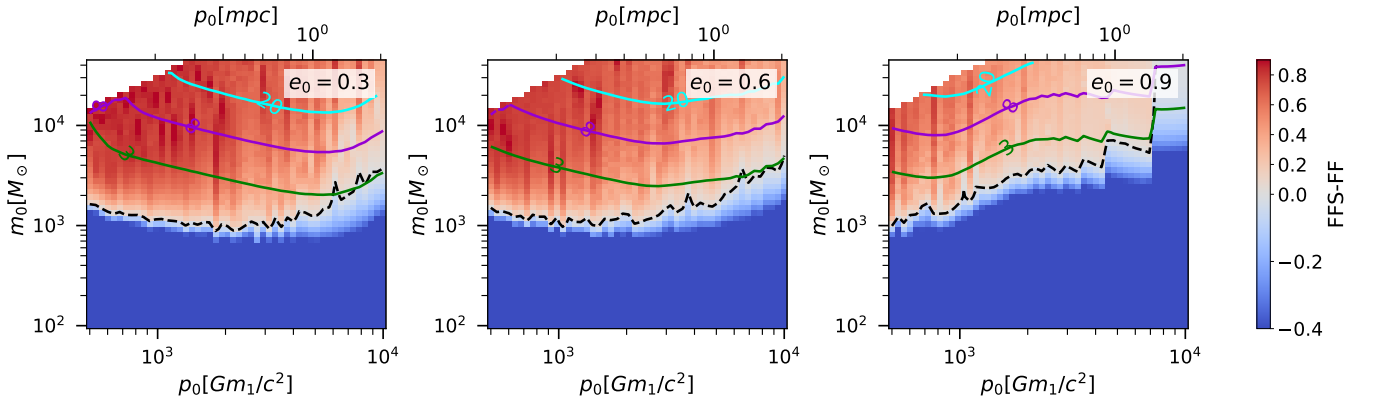


FIG. 12: We consider a small BH in an elliptical orbit within a DM spike characterized by a power-law slope of $\gamma_{\text{sp}} = 2.5$ in Eq. (7), which formed by a gNFW profile with $\gamma = 2$ in Eq. (4). The horizontal axis shows the semi-latus rectum p_0 , while the vertical axis represents the mass m_0 of the small BH. The green, purple, and cyan contour lines correspond to SNR values of 3, 8, and 20, respectively. The white translucent region in the upper left corner indicates where the small BH's orbit radius $r = p/(1 + e \cos \phi) < r_{\text{ISCO}}$ within the 30-year evolution timescale. The color bar represents the FFS-FF, where red regions indicate significant detectable differences in gravitational waveforms, blue regions correspond to undetectably small differences, and silver-white regions represent the detection threshold, the dashed line represents the FFS-FF = 0 contour.

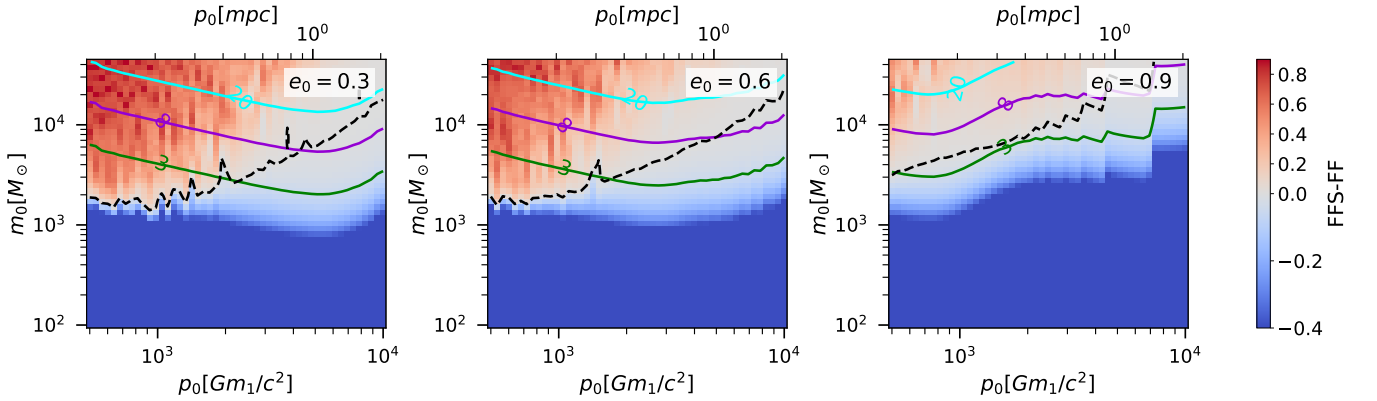


FIG. 13: DM density profile with $\gamma = 1.5$ under the gNFW profile in Eq. (4), forming a spike with $\gamma_{\text{sp}} = 2.4$ in Eq. (7), due to adiabatic compression by the central SMBH. The horizontal axis represents the semi-latus rectum p of the orbit, while the vertical axis shows the mass of the small BH. The color bar indicates the FFS-FF (GW waveform mismatch), with green, purple, and cyan contour lines corresponding to SNR of 3, 8, and 20, respectively.

indicating more pronounced waveform differences in GWs from BBH systems under DMr's gravitational influence. The transparent area in the figure's upper left corner corresponds to binary systems reaching $r < r_{\text{ISCO}}$ within 30 years, which we exclude from analysis. However, neighboring regions where BHs become closely separated may also yield less accurate GW calculations.

For $e_0 = 0.3$, SKA-PTA is most sensitive at 1 mpc. Around this region, we observe that a mass $m_0 \gtrsim 2000M_\odot$ yields $\text{SNR} > 3$, while a precise detection with $\text{SNR} = 8$ requires $m_0 \gtrsim 5000M_\odot$. For $e_0 = 0.6$, the highest sensitivity occurs at 0.5 mpc, where a mass $m_0 \gtrsim 2000M_\odot$ is detectable, and a precise detection requires $m_0 \gtrsim 6000M_\odot$. For $e_0 = 0.9$, the optimal sensitivity is at 0.2 mpc, where a mass $m_0 \gtrsim 3000M_\odot$ achieves $\text{SNR} = 3$, while a mass $m_0 \gtrsim 7000M_\odot$ is needed for $\text{SNR} = 8$.

The case of a spike with $\gamma_{\text{sp}} = 2.4$ is shown in Fig. 13. For $e_0 = 0.3$, the area above the dashed line represents waveform differences, where scattered black dots in the white region appear due to FF approaching unity and FFS also nearing unity at sufficient SNR, causing FFS-FF values to fluctuate around zero. Compared to $\gamma_{\text{sp}} = 2.5$, the $\gamma_{\text{sp}} = 2.4$ case shows that for eccentricities $e_0 = 0.3$ and 0.6 , the black dashed line imposes constraints, making it impossible to detect waveform differences at SKA-PTA's most sensitive regions. The area of the red zone is significantly reduced, and its depth is also diminished. A mass $m_0 \gtrsim 4000M_\odot$ near a semi-latus rectum of 0.2 mpc can achieve $\text{SNR} \gtrsim 3$,

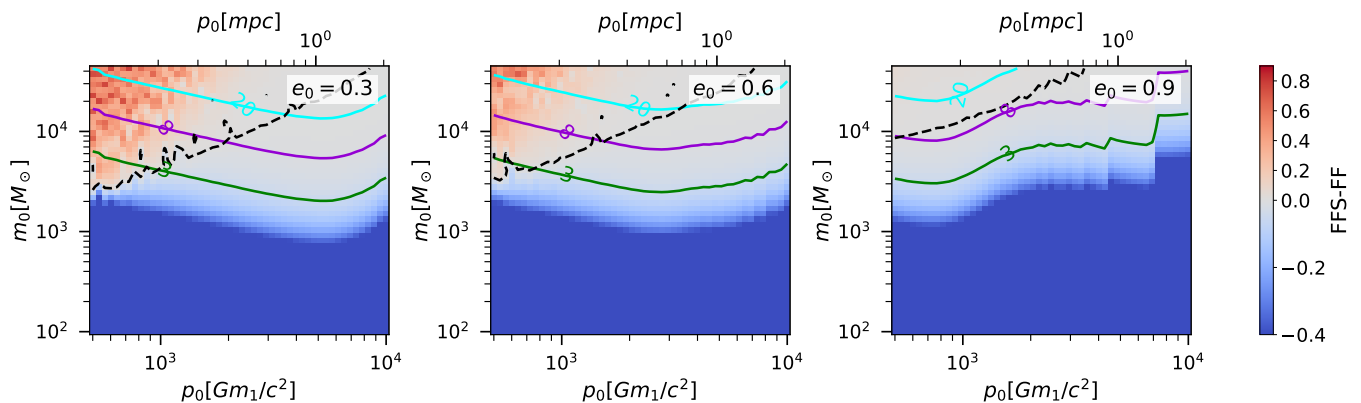


FIG. 14: DM density profile with $\gamma = 1$ under the gNFW profile in Eq. (4), forming a spike with $\gamma_{\text{sp}} = 7/3$ due to adiabatic compression by the central SMBH. The horizontal axis represents the semi-latus rectum p of the orbit, while the vertical axis shows the mass m_0 of the small BH. The color bar indicates the FFS-FF (GW waveform mismatch), with green, purple, and cyan contour lines corresponding to SNR of 3, 8, and 20, respectively.

while a mass $m_0 \gtrsim 7000M_\odot$ around 0.5 mpc reaches $\text{SNR} \gtrsim 8$. For $e_0 = 0.9$, since the black dashed line lies above the $\text{SNR}=3$ contour, the required mass is $m_0 \gtrsim 10^4 M_\odot$ at $p_0 \lesssim 0.2$ mpc.

We initially omitted the results for $\gamma = 1$ and $\gamma = 0$ cases because their lower DM densities resulted in $\text{FFS-FF} < 0$ throughout our parameter space, rendering the DM effects undetectable within a 30-year observation window. Fig. 14 displays the post-spike formation scenario for $\gamma = 1$ ($\gamma_{\text{sp}} = 7/3$). For systems with eccentricities of 0.3 and 0.6, waveform differences become observable when $m_0 \gtrsim 4000M_\odot$ near semi-latus rectum values of 0.2 mpc. Reliable detection within $\text{SNR} \geq 8$ requires satisfying both the constraint $p_0 \lesssim 0.4$ mpc imposed by the dashed line and maintaining masses above $10^4 M_\odot$. For $e_0 = 0.9$, we observe that the dashed line has shifted upward above the $\text{SNR}=8$ contour. Moreover, the region above the dashed line appears entirely silver-white, showing no discernible waveform differences in the plot.

Fig. 15 presents the post-spike scenario for $\gamma = 0.5$ with a resultant power-law index $\gamma_{\text{sp}} = 16/7$. In this case, detectable waveform differences emerge only in the upper-left parameter space region where $m_0 > 2 \times 10^4 M_\odot$ and $p_0 \lesssim 0.2$ mpc for the initial eccentricity $e_0 = 0.3$. For higher eccentricities, the entire detectable parameter space within SKA-PTA's sensitivity appears silvery-white, indicating that longer observation times would be required. Our results demonstrate that if the MW's initial DM distribution followed $\gamma = 0.5$, the combined effects of dynamical friction and accretion from the resulting spike profile would remain undetectable within a 30-year observation window.

In the Appendix A, we present GC-PTA detection results for spike profiles with $\gamma_{\text{sp}} = 2.5$ and 2.4, as shown in Figs. 17 and 18 respectively. For eccentricities $e_0 = 0.3$ and 0.6, we can detect BHs with masses $m_0 \sim 200M_\odot$ at orbital semi-latus recta around $p_0 = 0.2$ mpc. For the cases with $\gamma_{\text{sp}} = 7/3$ and 16/7, as shown in Figs. 19 and 20, the dashed constraints shift downward compared to SKA-PTA results, expanding the parameter space where $\text{FFS-FF} > 0$. However, due to weaker DM effects ($\text{FF} \approx 1$), the broadened parameter space remains silver-white in the plots, indicating no observable waveform differences.

V. CONCLUSIONS

In this work, we investigate the influence of DM environments on the elliptical orbits of BBHs to probe the DM distribution at the GC. Orbital modifications due to DM induce deviations in the gravitational waveform, with our analysis focusing primarily on the PTA frequency band. We examine various power-law inner slopes of the gNFW profile, as well as the resulting DM distribution after spike formation, and identify which slopes allow detectable DM effects within a 30-year observation window using SKA-PTA. Constraints are derived for these slope parameters. For detectable cases, we further constrain the parameter space of low-mass BHs.

In particular, we investigate the density profile of DM with different power-law indices γ in gNFW profile in Eq. (4). Under these constraints that, the total DM mass within the MW's virial radius r_{200} is $M_{\text{DM}}^{200} \approx 1.0 \times 10^{12} M_\odot$, and a local DM density near the Solar System is $\rho(r_\odot) = \rho_\odot = 0.4 \text{ GeV/cm}^3$, we consider the adiabatic compression of DM within the gravitational influence radius of the SMBH at the GC, which forms a DM spike in Eq. (7) and significantly enhances the DM distribution in this region. We subsequently delve into the scenario of elliptical orbits, in which a secondary BH situated within a DM environment undergoes alterations in both its orbital semi-latus rectum p and

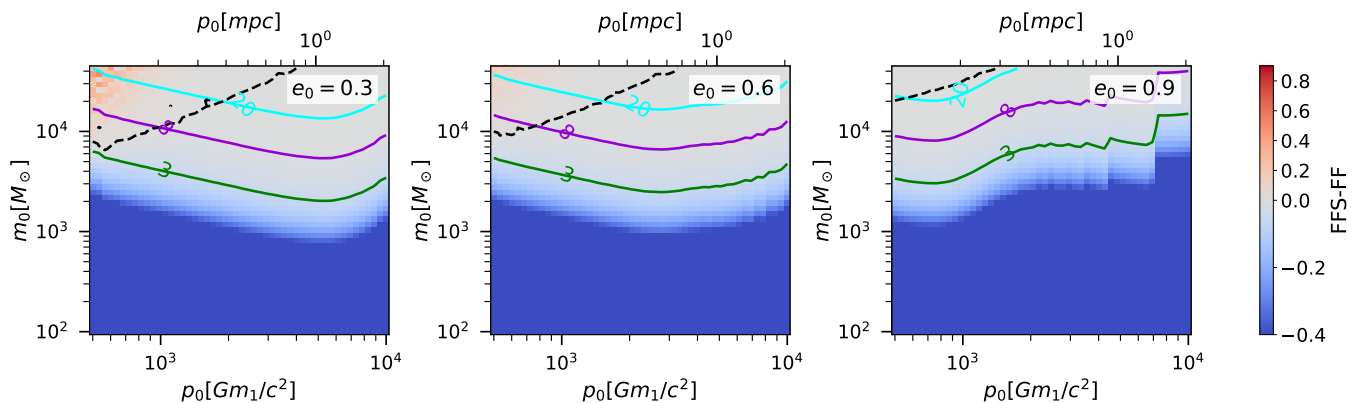


FIG. 15: DM density profile with $\gamma = 0.5$ under the gNFW profile in Eq. (4), forming a DM spike in Eq. (7) with $\gamma_{\text{sp}} = 16/7$ due to adiabatic compression by the central SMBH. The horizontal axis represents the semi-latus rectum p_0 of the orbit, while the vertical axis shows the mass m_0 of the small BH. The color bar indicates the FFS-FF (GW waveform mismatch), with green, purple, and cyan contour lines corresponding to SNR of 3, 8, and 20, respectively.

eccentricity e as a result of GW radiation. Simultaneously, the orbit is also affected by dynamical friction and DM accretion, which further alter these orbital parameters.

Our analysis shows that while GW radiation tends to decrease orbital eccentricity e , the presence of DM increases it. For the same initial eccentricity e_0 , this enhancement becomes more pronounced with higher DM densities and larger initial semi-latus rectum values. For initial semi-latus rectum values of $p_0 = 1000 Gm_1/c^2$ (~ 0.2 mpc) and $5000 Gm_1/c^2$ (~ 1 mpc), we observe that the orbital evolution under gNFW profiles in Eq. (4) with $\gamma = 1$ and 0.5 shows little difference compared to the DM-free case. However, when a DM spike in Eq. (7) is present, significant differences in the orbital evolution become apparent.

The DM environment exerts dynamical friction and accretion effects on orbiting BHs, causing deviations from DM-free orbital motion that manifest in gravitational waveforms. We examine whether different DM distributions affect secondary BHs detectably within 30-year observations, identifying parameter spaces (secondary BH masses and semi-latus rectum values) where waveform differences are most observable. To quantify detectability, we compute the frequency-domain inner product between waveforms with and without DM effects. By setting a threshold FFS, we determine when differences become observable, and present SNR contours delineating detectable parameter spaces. Our primary analysis uses SKA-PTA, with GC-PTA results in Appendix A. Our study using SKA-PTA over a 30-year observation period demonstrates that detecting DM effects requires both $\text{FFS-FF} > 0$ and $\text{SNR} \gtrsim 8$, while favoring smaller masses for the secondary BH probe. The detection thresholds for different DM distributions are as follows:

For the gNFW profile in Eq. (4) with $\gamma = 2$, systems with eccentricities $e_0 = 0.3$ and 0.6 require $m_0 \gtrsim 8000 M_\odot$ when $p_0 \approx 0.5$ mpc. While for $e_0 = 0.9$, the same mass threshold applies but only when $p_0 \lesssim 0.2$ mpc. Other gNFW profiles remain undetectable within the 30-year timeframe across the entire parameter space. For spike profiles in Eq. (7), the results show a strong dependence on γ_{sp} : When $\gamma_{\text{sp}} = 2.5$, the minimum mass requirements are $m_0 \gtrsim 5000 M_\odot$ for $e_0 = 0.3$ ($p_0 \approx 1$ mpc), $m_0 \gtrsim 6000 M_\odot$ for $e_0 = 0.6$ ($p_0 \approx 0.5$ mpc), and $m_0 \gtrsim 7000 M_\odot$ for $e_0 = 0.9$ ($p_0 \approx 0.2$ mpc). For $\gamma_{\text{sp}} = 2.4$, these increase to $m_0 \gtrsim 7000 M_\odot$ ($e_0 = 0.3$, $p_0 \approx 0.5$ mpc), $m_0 \gtrsim 7000 M_\odot$ ($e_0 = 0.6$, $p_0 \approx 0.4$ mpc), and $m_0 \gtrsim 8000 M_\odot$ ($e_0 = 0.9$, $p_0 \approx 0.2$ mpc). The steeper $\gamma_{\text{sp}} = 7/3$ profile demands $m_0 \gtrsim 10^4 M_\odot$ for $e_0 = 0.3$ and 0.6 when $p_0 \approx 0.2$ mpc, while showing no detectable signal for $e_0 = 0.9$. For the extreme case of $\gamma_{\text{sp}} = 16/7$, detection is only possible for $e_0 = 0.3$ with $p_0 \approx 0.1$ mpc, requiring $m_0 \gtrsim 2 \times 10^4 M_\odot$, with other eccentricities remaining undetectable.

These findings highlight how detection feasibility depends critically on both the DM density profile slope and the orbital parameters, with steeper profiles and higher eccentricities generally requiring more massive perturbers in tighter orbits for successful detection. For GC-PTA, when $\gamma = 2$ in the gNFW profile with eccentricities $e_0 = 0.3, 0.6$, the mass can be reduced to around $300 M_\odot$ near $p_0 = 0.2$ mpc. For spikes with $\gamma_{\text{sp}} = 2.5, 2.4$, GC-PTA can detect even smaller BHs. For other distributions, GC-PTA does not show significant advantages.

Beyond waveform predictions, our study provides explicit criteria for identifying detectable DM imprints, thereby enabling observational constraints on the underlying DM distribution. Although there could not exist the secondary massive BH in GC, there could be exist the secondary massive BH in the center of other nearby galaxies, i.e. M31, M32, M33, Large Magellanic Cloud, M87 and so on [67, 90, 94, 101]. The same methods can be also extended on the center of other nearby galaxies to constrain inner slope of DM profile. The GW signals from massive BBHs in nearby GCs offer an independent probe of the inner DM density profile slope. These observations can simultaneously

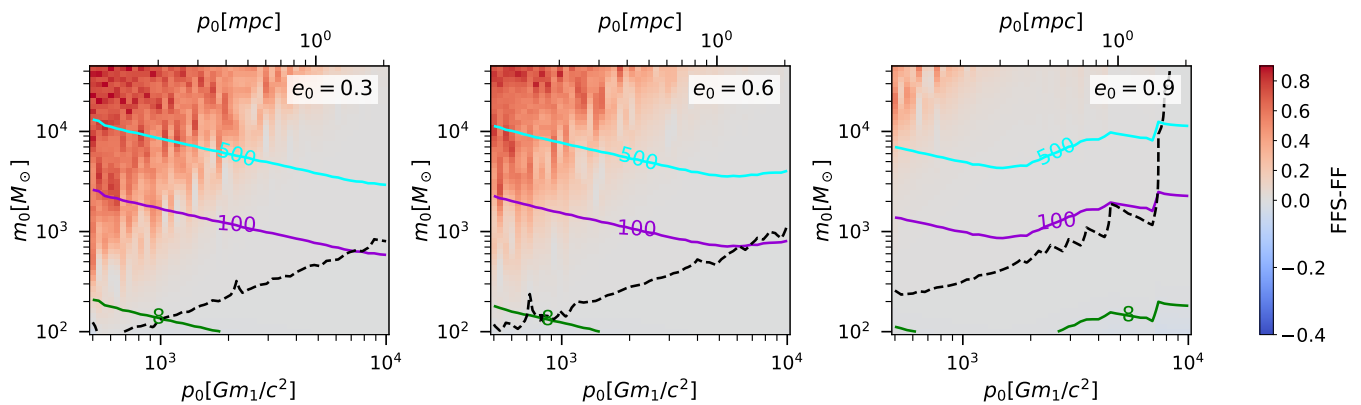


FIG. 16: The parameter space for secondary BH detection using GC-PTA under the gNFW DM profile in Eq. (4) with power-law slope $\gamma = 2$. The x-axis shows the semi-latus rectum p_0 while the y-axis represents mass m_0 . The FFS-FF metric quantifies GW waveform distortion significance caused by DM perturbations to BH orbits. Color coding indicates detectability over a 30-year observation period: red (detectable), silver (marginal detection threshold), and blue (undetectable).

constrain DM models and shed light on the nature of DM. Future studies could combine our results with galactic rotation curves and gravitational lensing data to provide multi-messenger constraints on DM properties.

ACKNOWLEDGMENTS

This work is supported by the National Key Research and Development Program of China (Nos. 2021YFC2203001, 2021YFC2201901), the National Natural Science Foundation of China (No.12375059), the fellowship of China National Postdoctoral Program for Innovative Talents (Grant No. BX20230104), and the Project of National Astronomical Observatories, Chinese Academy of Sciences (No. E4TG6601).

Appendix A: Galactic Center Pulsar Timing Array (GC-PTA)

If MSPs exist within the MW, we can discover them using SKA and utilize them as PTA to detect low-frequency GWs. We designate this configuration as GC-PTA, which offers significantly higher SNR compared to conventional extragalactic PTAs. We assume there are 10 MSPs in the MW. The SNR is calculated using Eq. (47) with $N_p = 10$, where the geometric factor χ is given by $\chi \approx 0.365 \left(\frac{r}{r_{pl}}\right) \approx 2920 \left(\frac{r}{8 \text{ kpc}}\right) \left(\frac{r_{pl}}{1 \text{ pc}}\right)^{-1}$ [90]. Here we assume that all 10 MSPs are located at distances $r \sim 1 \text{ pc}$ from the GC. In Eq. (48), we adopt the parameters $\sigma = 100 \text{ ns}$, $\Delta t = 0.02 \text{ yr}$, and $T = 30 \text{ yr}$. In this section, the figures demonstrate the waveform variations FFS-FF and SNR for GWs from the secondary BHs within different DM density profiles, as detected by the GC-PTA.

As shown in Fig. 16, if we do not consider DM spike formation, the GC-PTA demonstrates superior detection capabilities with higher SNR. Compared to SKA-PTA, GC-PTA can probe a larger parameter space within the 30-year observation window, with no undetectable regions (blue) in our selected parameter space. The analysis reveals significant DM effects for $\gamma = 2$, while for $\gamma = 1.5$ the FFS-FF values remain near the detection threshold indicating weaker DM influence. For even smaller power-law indices, the effects become negligible and are therefore not presented in Appendix A.

As shown in Figs. 17, 18, 19, and 20, these represent spikes formed from gNFW profiles with $\gamma = \{2, 1.5, 1, 0.5\}$ respectively, resulting in power-law indices $\gamma_{sp} = \{2.5, 2.4, 7/3, 16/7\}$. When DM forms a spike in Eq. (7), its density and power-law index increase significantly. Compared to SKA-PTA, the GC-PTA demonstrates the capability to detect the entire selected parameter space with significantly broader coverage.

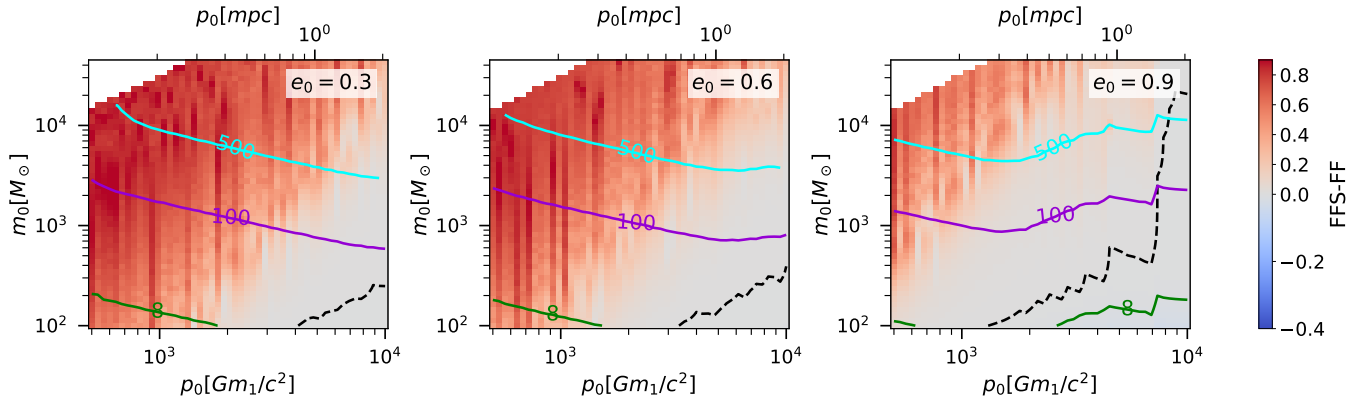


FIG. 17: FFS-FF and SNR of GWs by the GC-PTA, for the DM spike in Eq. (7) with $\gamma_{\text{sp}} = 2.5$, formed by the gNFW profile with $\gamma = 2$ in Eq. (4).

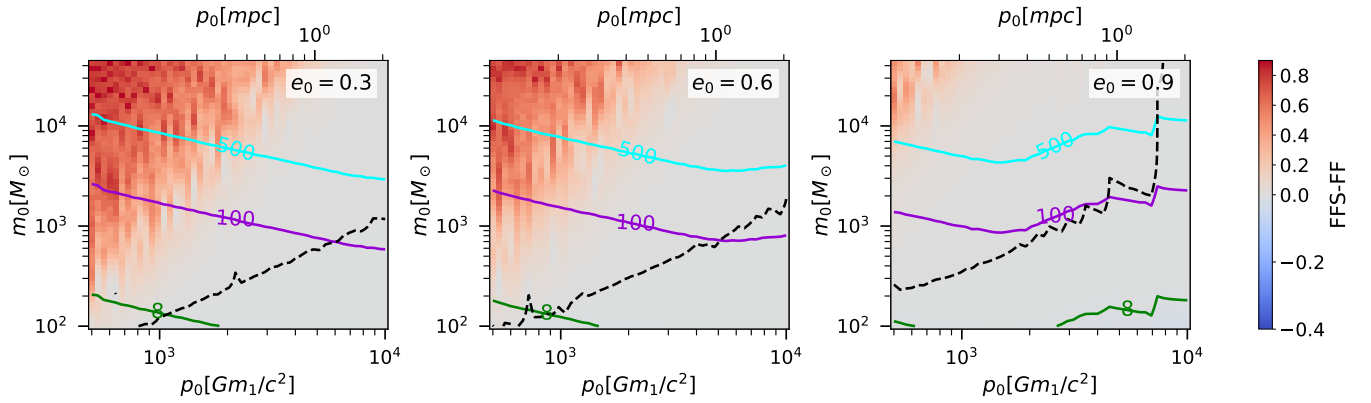


FIG. 18: FFS-FF and SNR of GWs by the GC-PTA, for the DM spike in Eq. (7) with $\gamma_{\text{sp}} = 2.4$, formed by the gNFW profile with $\gamma = 1.5$ in Eq. (4).

-
- [1] V. C. Rubin and W. K. Ford, Jr., Rotation of the Andromeda Nebula from a Spectroscopic Survey of Emission Regions, *Astrophys. J.* **159**, 379 (1970).
 - [2] D. Clowe, M. Bradac, A. H. Gonzalez, M. Markevitch, S. W. Randall, C. Jones, and D. Zaritsky, A direct empirical proof of the existence of dark matter, *Astrophys. J. Lett.* **648**, L109 (2006), [arXiv:astro-ph/0608407](#).
 - [3] P. A. R. Ade *et al.* (Planck), Planck 2015 results. XIII. Cosmological parameters, *Astron. Astrophys.* **594**, A13 (2016), [arXiv:1502.01589 \[astro-ph.CO\]](#).
 - [4] J. F. Navarro, C. S. Frenk, and S. D. M. White, The Structure of cold dark matter halos, *Astrophys. J.* **462**, 563 (1996), [arXiv:astro-ph/9508025](#).
 - [5] J. F. Navarro, C. S. Frenk, and S. D. M. White, A Universal density profile from hierarchical clustering, *Astrophys. J.* **490**, 493 (1997), [arXiv:astro-ph/9611107](#).
 - [6] B. Moore, T. R. Quinn, F. Governato, J. Stadel, and G. Lake, Cold collapse and the core catastrophe, *Mon. Not. Roy. Astron. Soc.* **310**, 1147 (1999), [arXiv:astro-ph/9903164](#).
 - [7] Y. P. Jing and Y. Suto, Density profiles of dark matter halo are not universal, *Astrophys. J. Lett.* **529**, L69 (2000), [arXiv:astro-ph/9909478](#).
 - [8] J. Wang, S. Bose, C. S. Frenk, L. Gao, A. Jenkins, V. Springel, and S. D. M. White, Universal structure of dark matter haloes over a mass range of 20 orders of magnitude, *Nature* **585**, 39 (2020), [arXiv:1911.09720 \[astro-ph.CO\]](#).
 - [9] R. A. Flores and J. R. Primack, Observational and theoretical constraints on singular dark matter halos, *Astrophys. J. Lett.* **427**, L1 (1994), [arXiv:astro-ph/9402004](#).
 - [10] B. Moore, Evidence against dissipationless dark matter from observations of galaxy haloes, *Nature* **370**, 629 (1994).
 - [11] S. Tulin and H.-B. Yu, Dark matter self-interactions and small scale structure, *Physics Reports* **730**, 1 (2018), [arXiv:1705.02358 \[hep-ph\]](#).
 - [12] P. Gondolo and J. Silk, Dark matter annihilation at the galactic center, *Phys. Rev. Lett.* **83**, 1719 (1999), [arXiv:astro-](#)

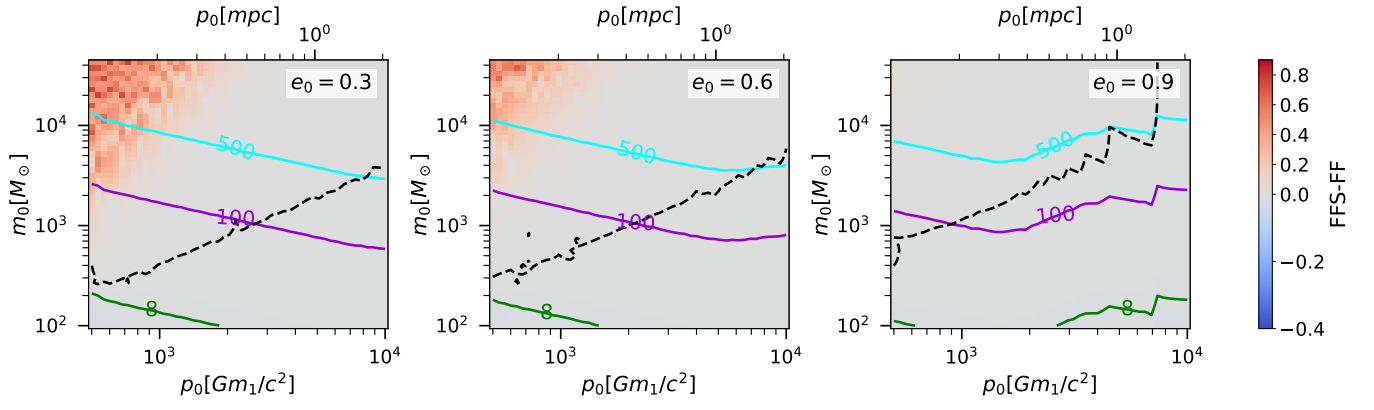


FIG. 19: FFS-FF and SNR of GWs by the GC-PTA, for the DM spike in Eq. (7) with $\gamma_{\text{sp}} = 7/3$, formed by the gNFW profile with $\gamma = 1$ in Eq. (4).

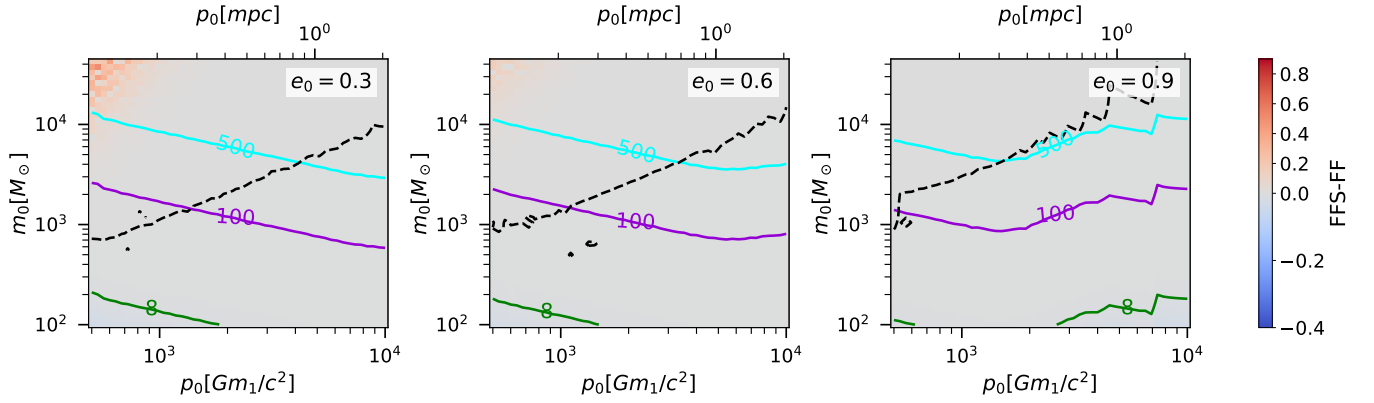


FIG. 20: FFS-FF and SNR of GWs by the GC-PTA, for the DM spike in Eq. (7) with $\gamma_{\text{sp}} = 16/7$, formed by the gNFW profile with $\gamma = 0.5$ in Eq. (4).

ph/9906391.

- [13] P. Ullio, H. Zhao, and M. Kamionkowski, A Dark matter spike at the galactic center?, *Phys. Rev. D* **64**, 043504 (2001), [arXiv:astro-ph/0101481](#).
- [14] D. Merritt, M. Milosavljevic, L. Verde, and R. Jimenez, Dark matter spikes and annihilation radiation from the galactic center, *Phys. Rev. Lett.* **88**, 191301 (2002), [arXiv:astro-ph/0201376](#).
- [15] D. Merritt, Evolution of the dark matter distribution at the galactic center, *Physical Review Letters* **92**, 201304 (2004).
- [16] B. Balick and R. L. Brown, Intense sub-arcsecond structure in the galactic center, *Astrophysical Journal*, vol. 194, Dec. 1, 1974, pt. 1, p. 265-270. **194**, 265 (1974).
- [17] R. Schodel *et al.*, A Star in a 15.2 year orbit around the supermassive black hole at the center of the Milky Way, *Nature* **419**, 694 (2002), [arXiv:astro-ph/0210426](#).
- [18] A. M. Ghez *et al.*, The first measurement of spectral lines in a short - period star bound to the galaxy's central black hole: A paradox of youth, *Astrophys. J. Lett.* **586**, L127 (2003), [arXiv:astro-ph/0302299](#).
- [19] R. Genzel, F. Eisenhauer, and S. Gillessen, The Galactic Center Massive Black Hole and Nuclear Star Cluster, *Rev. Mod. Phys.* **82**, 3121 (2010), [arXiv:1006.0064 \[astro-ph.GA\]](#).
- [20] M. Micic, K. Holley-Bockelmann, S. Sigurdsson, and T. Abel, Supermassive black hole growth and merger rates from cosmological n-body simulations, *Monthly Notices of the Royal Astronomical Society* **380**, 1533 (2007).
- [21] Y. Wang and B. Zhang, Evidence of a past merger of the galactic centre black hole, *Nature Astronomy*, 1 (2024).
- [22] D. Hooper and L. Goodenough, Dark matter annihilation in the galactic center as seen by the fermi gamma ray space telescope, *Physics Letters B* **697**, 412 (2011).
- [23] M. Ackermann, M. Ajello, A. Albert, B. Anderson, W. Atwood, L. Baldini, G. Barbiellini, D. Bastieri, R. Bellazzini, E. Bissaldi, *et al.*, Updated search for spectral lines from galactic dark matter interactions with pass 8 data from the fermi large area telescope, *Physical Review D* **91**, 122002 (2015).
- [24] M. Di Mauro, Characteristics of the galactic center excess measured with 11 years of fermi-lat data, *Physical Review D* **103**, 063029 (2021).
- [25] I. Cholis, Y.-M. Zhong, S. D. McDermott, and J. P. Surdutovich, Return of the templates: Revisiting the galactic center

- excess with multimessenger observations, *Physical Review D* **105**, 103023 (2022).
- [26] Y. Sofue, Rotation curve and mass distribution in the galactic center—from black hole to entire galaxy—, *Publications of the Astronomical Society of Japan* **65**, 118 (2013).
- [27] Q. Yu and S. Tremaine, Ejection of hypervelocity stars by the (binary) black hole in the galactic center, *The Astrophysical Journal* **599**, 1129 (2003).
- [28] B. M. Hansen and M. Milosavljević, The need for a second black hole at the galactic center, *The Astrophysical Journal* **593**, L77 (2003).
- [29] E. Girma and A. Loeb, Astrometric detection of intermediate-mass black holes at the galactic centre, *Monthly Notices of the Royal Astronomical Society* **482**, 3669 (2019).
- [30] S. Naoz, C. M. Will, E. Ramirez-Ruiz, A. Hees, A. M. Ghez, and T. Do, A hidden friend for the galactic center black hole, sgr a, *The Astrophysical Journal Letters* **888**, L8 (2019).
- [31] R. Abuter, A. Amorim, M. Bauböck, J. Berger, H. Bonnet, W. Brandner, V. Cardoso, Y. Clénet, P. De Zeeuw, J. Dexter, *et al.*, Detection of the schwarzschild precession in the orbit of the star s2 near the galactic centre massive black hole, *Astronomy & Astrophysics* **636**, L5 (2020).
- [32] O. Straub, M. Bauböck, R. Abuter, N. Aimar, P. A. Seoane, A. Amorim, J. Berger, H. Bonnet, G. Bourdarot, W. Brandner, *et al.*, Where intermediate-mass black holes could hide in the galactic centre—a full parameter study with the s2 orbit, *Astronomy & Astrophysics* **672**, A63 (2023).
- [33] C. M. Will, S. Naoz, A. Hees, A. Tucker, E. Zhang, T. Do, and A. Ghez, Constraining a companion of the galactic center black hole sgr a, *The Astrophysical Journal* **959**, 58 (2023).
- [34] M. Maggiore, *Gravitational waves*, Vol. 2 (Oxford university press, 2008).
- [35] A. Sesana, A. Vecchio, and M. Volonteri, Gravitational waves from resolvable massive black hole binary systems and observations with pulsar timing arrays, *Monthly Notices of the Royal Astronomical Society* **394**, 2255 (2009).
- [36] A. Sesana and A. Vecchio, Gravitational waves and pulsar timing: stochastic background, individual sources and parameter estimation, *Classical and Quantum Gravity* **27**, 084016 (2010).
- [37] K. Lee, N. Wex, M. Kramer, B. Stappers, C. Bassa, G. Janssen, R. Karuppusamy, and R. Smits, Gravitational wave astronomy of single sources with a pulsar timing array, *Monthly Notices of the Royal Astronomical Society* **414**, 3251 (2011).
- [38] A. Sesana, Gravitational wave emission from binary supermassive black holes, *Classical and Quantum Gravity* **30**, 244009 (2013).
- [39] X.-J. Zhu, G. Hobbs, L. Wen, W. A. Coles, J.-B. Wang, R. M. Shannon, R. N. Manchester, M. Bailes, N. Bhat, S. Burke-Spolaor, *et al.*, An all-sky search for continuous gravitational waves in the parkes pulsar timing array data set, *Monthly Notices of the Royal Astronomical Society* **444**, 3709 (2014).
- [40] K. Schutz and C.-P. Ma, Constraints on individual supermassive black hole binaries from pulsar timing array limits on continuous gravitational waves, *Monthly Notices of the Royal Astronomical Society* **459**, 1737 (2016).
- [41] S. R. Taylor, S. Burke-Spolaor, P. T. Baker, M. Charisi, K. Islo, L. Z. Kelley, D. R. Madison, J. Simon, and S. Vigeland, Supermassive black-hole demographics & environments with pulsar timing arrays, *arXiv preprint arXiv:1903.08183* (2019).
- [42] G. Agazie, A. Anumarlapudi, A. M. Archibald, Z. Arzoumanian, P. T. Baker, B. Bécsy, L. Blecha, A. Brazier, P. R. Brook, S. Burke-Spolaor, *et al.*, The nanograv 15 yr data set: Bayesian limits on gravitational waves from individual supermassive black hole binaries, *The Astrophysical Journal Letters* **951**, L50 (2023).
- [43] J. Antoniadis, P. Arumugam, S. Arumugam, S. Babak, M. Bagchi, A.-S. B. Nielsen, C. Bassa, A. Bathula, A. Berthereau, M. Bonetti, *et al.*, The second data release from the european pulsar timing array-iv. implications for massive black holes, dark matter, and the early universe, *Astronomy & Astrophysics* **685**, A94 (2024).
- [44] B. P. Abbott *et al.* (LIGO Scientific, Virgo), Observation of Gravitational Waves from a Binary Black Hole Merger, *Phys. Rev. Lett.* **116**, 061102 (2016), [arXiv:1602.03837 \[gr-qc\]](https://arxiv.org/abs/1602.03837).
- [45] B. P. Abbott *et al.* (LIGO Scientific, Virgo), GW170817: Observation of Gravitational Waves from a Binary Neutron Star Inspiral, *Phys. Rev. Lett.* **119**, 161101 (2017), [arXiv:1710.05832 \[gr-qc\]](https://arxiv.org/abs/1710.05832).
- [46] B. P. Abbott *et al.*, Multi-messenger Observations of a Binary Neutron Star Merger, *Astrophys. J. Lett.* **848**, L12 (2017), [arXiv:1710.05833 \[astro-ph.HE\]](https://arxiv.org/abs/1710.05833).
- [47] B. P. Abbott *et al.* (LIGO Scientific, Virgo), GWTC-1: A Gravitational-Wave Transient Catalog of Compact Binary Mergers Observed by LIGO and Virgo during the First and Second Observing Runs, *Phys. Rev. X* **9**, 031040 (2019), [arXiv:1811.12907 \[astro-ph.HE\]](https://arxiv.org/abs/1811.12907).
- [48] G. Agazie *et al.* (NANOGrav), The NANOGrav 15 yr Data Set: Evidence for a Gravitational-wave Background, *Astrophys. J. Lett.* **951**, L8 (2023), [arXiv:2306.16213 \[astro-ph.HE\]](https://arxiv.org/abs/2306.16213).
- [49] A. Afzal *et al.* (NANOGrav), The NANOGrav 15 yr Data Set: Search for Signals from New Physics, *Astrophys. J. Lett.* **951**, L11 (2023), [Erratum: *Astrophys.J.Lett.* 971, L27 (2024), Erratum: *Astrophys.J.* 971, L27 (2024)], [arXiv:2306.16219 \[astro-ph.HE\]](https://arxiv.org/abs/2306.16219).
- [50] D. J. Reardon *et al.*, Search for an Isotropic Gravitational-wave Background with the Parkes Pulsar Timing Array, *Astrophys. J. Lett.* **951**, L6 (2023), [arXiv:2306.16215 \[astro-ph.HE\]](https://arxiv.org/abs/2306.16215).
- [51] H. Xu *et al.*, Searching for the Nano-Hertz Stochastic Gravitational Wave Background with the Chinese Pulsar Timing Array Data Release I, *Res. Astron. Astrophys.* **23**, 075024 (2023), [arXiv:2306.16216 \[astro-ph.HE\]](https://arxiv.org/abs/2306.16216).
- [52] J. Antoniadis *et al.* (EPTA, InPTA:), The second data release from the European Pulsar Timing Array - III. Search for gravitational wave signals, *Astron. Astrophys.* **678**, A50 (2023), [arXiv:2306.16214 \[astro-ph.HE\]](https://arxiv.org/abs/2306.16214).
- [53] G. Bertone *et al.*, Gravitational wave probes of dark matter: challenges and opportunities, *SciPost Phys. Core* **3**, 007 (2020), [arXiv:1907.10610 \[astro-ph.CO\]](https://arxiv.org/abs/1907.10610).

- [54] T. Lazio, The square kilometre array pulsar timing array, *Classical and Quantum Gravity* **30**, 224011 (2013).
- [55] Y. Wang and S. D. Mohanty, Pulsar timing array based search for supermassive black hole binaries in the square kilometer array era, *Physical review letters* **118**, 151104 (2017).
- [56] S. Chandrasekhar, Dynamical Friction. I. General Considerations: the Coefficient of Dynamical Friction, *Astrophys. J.* **97**, 255 (1943).
- [57] E. C. Ostriker, Dynamical friction in a gaseous medium, *Astrophys. J.* **513**, 252 (1999), [arXiv:astro-ph/9810324](#).
- [58] K. Eda, Y. Itoh, S. Kuroyanagi, and J. Silk, New Probe of Dark-Matter Properties: Gravitational Waves from an Intermediate-Mass Black Hole Embedded in a Dark-Matter Minispike, *Phys. Rev. Lett.* **110**, 221101 (2013), [arXiv:1301.5971 \[gr-qc\]](#).
- [59] K. Eda, Y. Itoh, S. Kuroyanagi, and J. Silk, Gravitational waves as a probe of dark matter minispikes, *Phys. Rev. D* **91**, 044045 (2015), [arXiv:1408.3534 \[gr-qc\]](#).
- [60] C. F. B. Macedo, P. Pani, V. Cardoso, and L. C. B. Crispino, Into the lair: gravitational-wave signatures of dark matter, *Astrophys. J.* **774**, 48 (2013), [arXiv:1302.2646 \[gr-qc\]](#).
- [61] X.-J. Yue and W.-B. Han, Gravitational waves with dark matter minispikes: the combined effect, *Phys. Rev. D* **97**, 064003 (2018), [arXiv:1711.09706 \[gr-qc\]](#).
- [62] X.-J. Yue and Z. Cao, Dark matter minispike: A significant enhancement of eccentricity for intermediate-mass-ratio inspirals, *Phys. Rev. D* **100**, 043013 (2019), [arXiv:1908.10241 \[astro-ph.HE\]](#).
- [63] B. J. Kavanagh, D. A. Nichols, G. Bertone, and D. Gaggero, Detecting dark matter around black holes with gravitational waves: Effects of dark-matter dynamics on the gravitational waveform, *Phys. Rev. D* **102**, 083006 (2020), [arXiv:2002.12811 \[gr-qc\]](#).
- [64] N. Dai, Y. Gong, T. Jiang, and D. Liang, Intermediate mass-ratio inspirals with dark matter minispikes, *Phys. Rev. D* **106**, 064003 (2022), [arXiv:2111.13514 \[gr-qc\]](#).
- [65] N. Becker, L. Sagunski, L. Prinz, and S. Rastgoo, Circularization versus eccentricification in intermediate mass ratio inspirals inside dark matter spikes, *Phys. Rev. D* **105**, 063029 (2022), [arXiv:2112.09586 \[gr-qc\]](#).
- [66] G.-L. Li, Y. Tang, and Y.-L. Wu, Probing dark matter spikes via gravitational waves of extreme-mass-ratio inspirals, *Sci. China Phys. Mech. Astron.* **65**, 100412 (2022), [arXiv:2112.14041 \[astro-ph.CO\]](#).
- [67] C. Feng, Y. Tang, and Y.-L. Wu, Probing Dark Matter Spike with Gravitational Waves from Early EMRIs in the Milky Way Center, *arXiv e-prints*, [arXiv:2506.02937 \(2025\)](#), [arXiv:2506.02937 \[astro-ph.GA\]](#).
- [68] N. Dai, Y. Gong, Y. Zhao, and T. Jiang, Extreme mass ratio inspirals in galaxies with dark matter halos, *Phys. Rev. D* **110**, 084080 (2024), [arXiv:2301.05088 \[gr-qc\]](#).
- [69] N. Speeney, A. Antonelli, V. Baibhav, and E. Berti, Impact of relativistic corrections on the detectability of dark-matter spikes with gravitational waves, *Phys. Rev. D* **106**, 044027 (2022), [arXiv:2204.12508 \[gr-qc\]](#).
- [70] N. Becker and L. Sagunski, Comparing accretion disks and dark matter spikes in intermediate mass ratio inspirals, *Phys. Rev. D* **107**, 083003 (2023), [arXiv:2211.05145 \[gr-qc\]](#).
- [71] P. S. Cole, G. Bertone, A. Coogan, D. Gaggero, T. Karydas, B. J. Kavanagh, T. F. M. Spieksma, and G. M. Tomaselli, Distinguishing environmental effects on binary black hole gravitational waveforms, *Nature Astron.* **7**, 943 (2023), [arXiv:2211.01362 \[gr-qc\]](#).
- [72] D. Shadykul, H. Chakrabarty, and D. Malafarina, Intermediate mass ratio inspirals in dark matter halos, *Phys. Rev. D* **111**, 104003 (2025), [arXiv:2410.18657 \[gr-qc\]](#).
- [73] M. Daniel, K. Pardo, and L. Sagunski, Forecasted detection limits on the (dark) matter density in supermassive black hole binaries for lisa, *arXiv preprint arXiv:2501.13601* (2025).
- [74] A. M. Ghez, S. Salim, N. Weinberg, J. Lu, T. Do, J. Dunn, K. Matthews, M. Morris, S. Yelda, E. Becklin, *et al.*, Measuring distance and properties of the milky way's central supermassive black hole with stellar orbits, *The Astrophysical Journal* **689**, 1044 (2008).
- [75] R. Abuter *et al.* (GRAVITY), Mass distribution in the Galactic Center based on interferometric astrometry of multiple stellar orbits, *Astron. Astrophys.* **657**, L12 (2022), [arXiv:2112.07478 \[astro-ph.GA\]](#).
- [76] Y. Sofue, Rotation curve of the milky way and the dark matter density, *Galaxies* **8**, 37 (2020).
- [77] M. Cirelli, A. Strumia, and J. Zupan, Dark matter, *arXiv preprint arXiv:2406.01705* (2024).
- [78] M. Cautun, A. Benitez-Llambay, A. J. Deason, C. S. Frenk, A. Fattahi, F. A. Gómez, R. J. J. Grand, K. A. Oman, J. F. Navarro, and C. M. Simpson, The Milky Way total mass profile as inferred from Gaia DR2, *Mon. Not. Roy. Astron. Soc.* **494**, 4291 (2020), [arXiv:1911.04557 \[astro-ph.GA\]](#).
- [79] J. Diemand, M. Kuhlen, P. Madau, M. Zemp, B. Moore, D. Potter, and J. Stadel, Clumps and streams in the local dark matter distribution, *Nature* **454**, 735 (2008), [arXiv:0805.1244 \[astro-ph\]](#).
- [80] R. Abuter, A. Amorim, M. Bauböck, J. Berger, H. Bonnet, W. Brandner, Y. Clénet, V. C. Du Foresto, P. De Zeeuw, J. Dexter, *et al.*, A geometric distance measurement to the galactic center black hole with 0.3% uncertainty, *Astronomy & Astrophysics* **625**, L10 (2019).
- [81] R. Schödel, T. Ott, R. Genzel, R. Hofmann, M. Lehnert, A. Eckart, N. Mouawad, T. Alexander, M. Reid, R. Lenzen, *et al.*, A star in a 15.2-year orbit around the supermassive black hole at the centre of the milky way, *Nature* **419**, 694 (2002).
- [82] D. Merritt, Single and binary black holes and their influence on nuclear structure, in *Carnegie Observatories Centennial Symposium*. (2003) [arXiv:astro-ph/0301257](#).
- [83] E. Poisson and C. M. Will, *Gravity: Newtonian, post-newtonian, relativistic* (Cambridge University Press, 2014).
- [84] V. Cardoso, C. F. B. Macedo, and R. Vicente, Eccentricity evolution of compact binaries and applications to gravitational-wave physics, *Phys. Rev. D* **103**, 023015 (2021), [arXiv:2010.15151 \[gr-qc\]](#).

- [85] H. Kim and W.-T. Kim, Dynamical Friction of a Circular-Orbit Perturber in a Gaseous Medium, *Astrophys. J.* **665**, 432 (2007), [arXiv:0705.0084 \[astro-ph\]](#).
- [86] P. Mach and A. Odrzywo, Accretion of Dark Matter onto a Moving Schwarzschild Black Hole: An Exact Solution, *Phys. Rev. Lett.* **126**, 101104 (2021), [arXiv:2103.03595 \[gr-qc\]](#).
- [87] S. Husa, Michele maggiore: Gravitational waves. volume 1: theory and experiments, *General Relativity and Gravitation* **41**, 1667 (2009).
- [88] P. Jaranowski and A. Krolak, Analysis of gravitational-wave data, *Analysis of Gravitational-Wave Data*, by Piotr Jaranowski, Andrzej Krolak, Cambridge, UK: Cambridge University Press, 2009 (2009).
- [89] E. Gourgoulhon, A. Le Tiec, F. H. Vincent, and N. Warburton, Gravitational waves from bodies orbiting the Galactic Center black hole and their detectability by LISA, *Astron. Astrophys.* **627**, A92 (2019), [arXiv:1903.02049 \[gr-qc\]](#).
- [90] X. Guo, Y. Lu, and Q. Yu, On Detecting Nearby Nanohertz Gravitational Wave Sources via Pulsar Timing Arrays, *Astrophys. J.* **939**, 55 (2022), [arXiv:2209.05666 \[astro-ph.HE\]](#).
- [91] C. J. Moore, S. R. Taylor, and J. R. Gair, Estimating the sensitivity of pulsar timing arrays, *Class. Quant. Grav.* **32**, 055004 (2015), [arXiv:1406.5199 \[astro-ph.IM\]](#).
- [92] P. A. Rosado, A. Sesana, and J. Gair, Expected properties of the first gravitational wave signal detected with pulsar timing arrays, *Mon. Not. Roy. Astron. Soc.* **451**, 2417 (2015), [arXiv:1503.04803 \[astro-ph.HE\]](#).
- [93] J. M. Goldstein, A. Sesana, A. M. Holgado, and J. Veitch, Associating host galaxy candidates to massive black hole binaries resolved by pulsar timing arrays, *Mon. Not. Roy. Astron. Soc.* **485**, 248 (2019), [arXiv:1812.02670 \[astro-ph.IM\]](#).
- [94] Y. Chen, Q. Yu, and Y. Lu, Dynamical evolution of cosmic supermassive binary black holes and their gravitational wave radiation, *Astrophys. J.* **897**, 86 (2020), [arXiv:2005.10818 \[astro-ph.HE\]](#).
- [95] B. Goncharov, X.-J. Zhu, and E. Thrane, Is there a spectral turnover in the spin noise of millisecond pulsars?, *Mon. Not. Roy. Astron. Soc.* **497**, 3264 (2020), [arXiv:1910.05961 \[astro-ph.HE\]](#).
- [96] L. Lentati *et al.*, From Spin Noise to Systematics: Stochastic Processes in the First International Pulsar Timing Array Data Release, *Mon. Not. Roy. Astron. Soc.* **458**, 2161 (2016), [arXiv:1602.05570 \[astro-ph.IM\]](#).
- [97] J. D. E. Creighton and W. G. Anderson, *Gravitational-wave physics and astronomy: An introduction to theory, experiment and data analysis* (2011).
- [98] Y. Fang, X. Chen, and Q.-G. Huang, Impact of a spinning supermassive black hole on the orbit and gravitational waves of a nearby compact binary, *The Astrophysical Journal* **887**, 210 (2019).
- [99] T. A. Apostolatos, C. Cutler, G. J. Sussman, and K. S. Thorne, Spin induced orbital precession and its modulation of the gravitational wave forms from merging binaries, *Phys. Rev. D* **49**, 6274 (1994).
- [100] L. Lindblom, B. J. Owen, and D. A. Brown, Model Waveform Accuracy Standards for Gravitational Wave Data Analysis, *Phys. Rev. D* **78**, 124020 (2008), [arXiv:0809.3844 \[gr-qc\]](#).
- [101] X. Guo, Q. Yu, and Y. Lu, Constraining the Binarity of Massive Black Holes in the Galactic Center and Some Nearby Galaxies via Pulsar Timing Array Observations of Gravitational Waves, *Astrophys. J.* **978**, 104 (2025), [arXiv:2411.14150 \[astro-ph.HE\]](#).